



Contents lists available at ScienceDirect

Journal of Sound and Vibration

journal homepage: www.elsevier.com/locate/jsv



A novel model order reduction technique for solving horizontal refraction equations in the modeling of three-dimensional underwater acoustic propagation

Tengjiao He ^{a,1}, Juan Liu ^{b,*}, Shanjun Ye ^{a,1}, Xin Qing ^c, Shiqi Mo ^c

^a Key Laboratory of Marine Intelligent Equipment and System, Ministry of Education, Shanghai Jiao Tong University, Shanghai, 200240, PR China

^b College of Meteorology and Oceanography, National University of Defense Technology, Changsha, 410073, PR China

^c College of Underwater Acoustic Engineering, Harbin Engineering University, Harbin, 150001, PR China



ARTICLE INFO

Keywords:

Model order reduction
Horizontal refraction equations
Adiabatic approximation
Modal projection method
Normal mode theory
Three-dimensional underwater acoustic propagation

ABSTRACT

Modeling three-dimensional (3D) underwater acoustic propagation is vital for underwater detection, localization, and navigation. This article introduces a novel model order reduction (MOR) technique to solve horizontal refraction equations (HREs) in the modeling of 3D underwater acoustic propagation. This approach relies on an adiabatic approximation of the 3D sound field, representing the field as a combination of local vertical modes with their modal coefficients governed by a system of two-dimensional (2D) HREs. Inspired by normal mode theory, the coefficients in the expansion over vertical modes are determined by projecting them onto a lower-dimensional, orthogonal space defined by their transverse eigenfunctions. By artificially truncating the horizontal domain in the transverse directions using two perfectly matched layers (PMLs), the eigenproblem associated with the transverse eigenfunctions of the modal coefficients is closed and thus can be solved through a modal projection method. The modal projection method enables fast computation of modal coefficients in a longitudinally invariant environment within seconds, offering a naturally wide-angle solution covering $\pm 90^\circ$. The MOR method is extended to encompass fully 3D cases by introducing an admittance matrix, a memory-saving strategy that prevents numerical overflow when the longitudinal range is large. Moreover, the fact that the outer boundaries of the PMLs are range-independent allows the proposed MOR technique to perform well on a coarse grid when employing the Magnus scheme, significantly saving the numerical cost for the fully 3D simulation. Numerical simulations are provided for both longitudinally invariant and fully 3D scenarios, demonstrating the high accuracy and efficiency of the proposed MOR technique in solving HREs.

1. Introduction

The modeling of 3D underwater acoustic propagation is essential for acoustic localization, navigation, and detection under complex underwater conditions. Such modeling can provide crucial information about underwater acoustic environments, potentially enhancing sonar performance. The pivotal component of this modeling is solving the 3D Helmholtz equation, which is typically

* Corresponding author.

E-mail address: liujuan22@nudt.edu.cn (J. Liu).

¹ Also at: Collaborative Innovation Center for Advanced Ship and Deep-Sea Exploration, State Key Laboratory of Ocean Engineering, Shanghai Jiao Tong University, Shanghai 200240 PR China.

achieved through fully numerical methods on modern computer platforms. In recent years, there has been growing interest in such approaches, which include the finite element method (FEM) [1], the spectral element method [2,3], the finite difference method (FDM) [4], the boundary element method (BEM) [5], and the equivalent source method (ESM) [6]. These methods explicitly solve the 3D Helmholtz equation, introducing only discretization as an approximation. Consequently, they provide a full-wave solution that simultaneously accounts for high-order scattering, horizontal refraction and diffraction, and mode coupling effects. While these methods have proven powerful for studying and benchmarking 3D propagation effects, their computational efficiency remains a bottleneck, potentially limiting their applications due to limited computational resources.

However, a significant improvement in computational efficiency when solving the 3D Helmholtz equation can be achieved by introducing some degree of approximation, as exemplified by the parabolic equation. The standard form of the parabolic equation is derived through the paraxial approximation of the Helmholtz equation and simplifies the problem by omitting back-scattering and assuming that the boundary and the medium along the propagation range are slow-varying [7]. This simplification results in a one-way wave equation that evolves with distance. Pioneering work on the 3D parabolic equation was conducted by Baer [8], and subsequent authors have advanced various aspects, such as propagation angles, accuracy, and versatility in different coordinates [9–13]. With the support of parallel computing, 3D parabolic equations have been employed to analyze global-scale T-phase wave propagation [3,14–16] and to interpret propagation effects in complex ocean environments, including canyons [17–19] and regions around islands [20].

The solutions provided by the 3D parabolic equation accommodate both horizontal refraction and mode coupling effects. The latter has proven to be of secondary importance in many practical cases [21,22], particularly in environments dominated by horizontal refraction, such as coastal wedges and underwater canyons. By representing the 3D sound field through modal decomposition and neglecting mode coupling effects, one can reduce the 3D Helmholtz equation to an array of 2D Helmholtz-type equations governing the coefficients in the expansion over vertical modes. The 2D Helmholtz-type equations are the so-called *horizontal refraction equations* (HREs). They can be solved using ray theory [21], parabolic equations [22,23], or analytical approaches with restrictions on simulated environments [24–26]. Solving HREs is numerically more efficient than solving 3D parabolic equations, as they can be considered a model order reduction (MOR) method [22,27]. They represent the field in the vertical dimension as a combination of orthogonal vertical modes, typically discretized into at least several hundred points by the 3D parabolic equation (much larger than the number of vertical modes). The approaches described above for solving HREs involve approximations that could potentially introduce additional unwanted errors into the solution. Therefore, one could argue for solving HREs explicitly without introducing further approximations beyond the adiabatic (uncoupled) approximation into the 3D Helmholtz equation. One of the goals of this article is to develop such a method for exactly solving HREs.

In recent years, there has been significant interest in MOR techniques across the fields of computational mechanics, fluid dynamics, and acoustics [28–33]. These techniques have proven to be highly beneficial for enhancing numerical efficiency without compromising accuracy. In acoustics, MOR has been effectively employed to expedite a direct solver for linear equations in coupled FEM/BEM vibroacoustic formulations [34]. Similar methods have also found application in addressing sound scattering through a reduced BEM formula [35–37]. The fundamental principle of MOR involves spanning an orthogonal space with a set of basis functions onto which the original system of equations is projected. The projection enables the original problem to be solved using a very small system in the projection space so that the numerical efficacy can be improved significantly due to the reduced size. This is akin to the application of HREs in 3D underwater acoustic propagation described earlier. Recent research suggests that the concept of normal modes can be considered an early form of MOR [38].

Our second objective is to achieve MOR for the solution to HREs, inspired by normal mode theory. However, this is challenging as normal modes are typically employed in bounded spaces (such as cavities or waveguides) [7], while HREs are essentially 2D Helmholtz-type equations without boundary conditions in both the longitudinal and transverse directions. To address this, we construct an orthogonal space using transverse eigenfunctions of modal coefficients. These modal coefficients are then projected onto the space, allowing for a solution in a lower dimension with high efficiency. Subsequently, the transverse directions are artificially truncated by two perfectly matched layers (PMLs) [39] with actual outer boundaries, and the eigenproblem of the original open space for transverse eigenfunctions is closed by applying a modal projection method [40,41]. Our results demonstrate that the proposed MOR technique for solving HREs requires only a few seconds of computational time when the environment is longitudinally invariant. This represents a significant improvement, being a hundred times faster than state-of-the-art wide-angle mode parabolic equation [22].

This article presents a novel MOR technique for solving HREs to model 3D underwater acoustic propagation. Our model excludes mode coupling effects. Initially, we introduce modal decomposition to the 3D Helmholtz equation, expressing the sound field as a combination of local vertical modes whose coefficients are governed by a set of 2D HREs. Inspired by normal mode theory, our proposed MOR technique determines the modal coefficients by projecting them onto a lower-dimensional space spanned by their transverse eigenfunctions. We artificially truncate the transverse directions using two PMLs to absorb outgoing waves and eliminate branch-cut contributions resulting from the continuous spectrum. This closure of the eigenproblem associated with transverse eigenfunctions allows it to be solved using a modal projection method [40,41]. The modal projection method allows one to efficiently compute the modal coefficients, especially in longitudinally invariant underwater environments. The efficiency of the modal projection method arises from the variable separability of HREs in longitudinally invariant environments. Determining the modal coefficients becomes highly efficient, as the eigenproblem for their transverse eigenfunction is solved only once. Additionally, the solution provided by our proposed MOR is naturally wide-angle, covering horizontal angles $\pm 90^\circ$.

To extend our MOR technique to fully 3D environments, we introduce an admittance matrix [42–44] that converts an HRE with 2D inhomogeneous horizontal wavenumbers into a first-order evolution equation [45,46]. This enables the solving of coupled

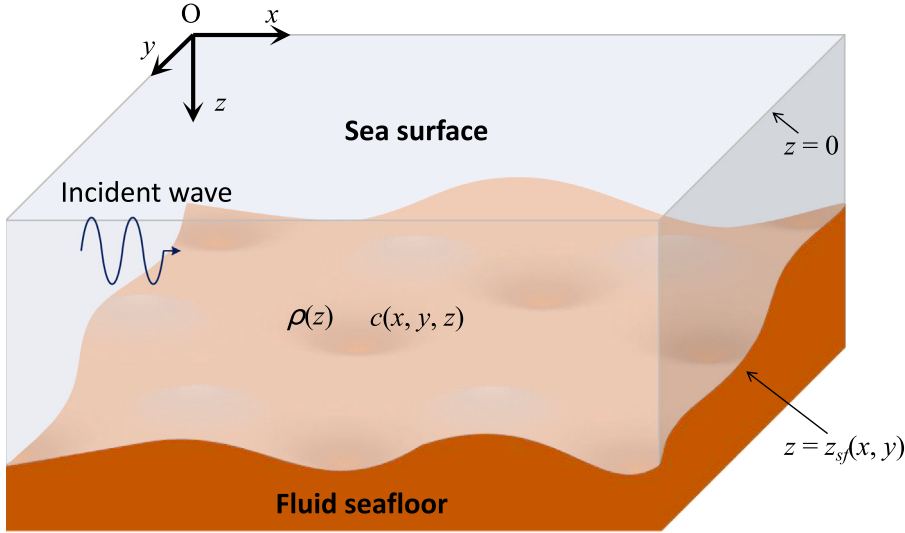


Fig. 1. A schematic of the 3D underwater environment considered in the current analysis, showing the medium sound speed as a function of the spatial coordinates (x, y, z) . The medium density depends only on the depth. The sea surface is located on the $z = 0$ plane, and the seafloor is described as $z_{sf}(x, y)$, i.e., by a fully 2D function.

transverse eigenfunctions of modal coefficients, circumventing the numerical overflow associated with the global matrix method. Additionally, the fact that the outer boundaries of the PMLs are range-independent enables the proposed MOR technique to excel with a coarse grid when utilizing the Magnus scheme to solve the evolution equation, thus reducing numerical costs for fully 3D simulations. Numerical simulations are performed that cover both longitudinally invariant and fully 3D scenarios, including coastal wedges, cosine hills, and oceans over corrugated seafloors and realistic topography. The results validate the ability of the proposed MOR technique to solve HREs and 3D underwater acoustic propagation and affirm its high efficiency, especially in longitudinally invariant environments. This technique could be useful in various future applications, particularly for modeling acoustic radiation or scattering from submerged objects and conducting time-domain simulations.

The remainder of this paper is organized as follows. Section 2 presents the equations characterizing the MOR technique, including the governing equations of the 3D sound field and the formulation of the modal projection method and the admittance matrix. Section 3 presents numerical simulations, including validation cases and analyses of the suitability of the proposed model. Finally, conclusions are drawn in Section 4.

2. An exact solver for horizontal refraction equations based on model order reduction

As shown in Fig. 1, a standard ocean waveguide environment is analyzed, in which the medium density $\rho(z)$ is assumed to depend solely on the depth z . The sound speed of the medium, denoted as $c(x, y, z)$, varies with the 3D spatial coordinates (x, y, z) . The ocean surface is situated at $z = 0$, and the interface between the water and seafloor is defined as $z = z_{sf}(x, y)$. Here, the governing equations for the 3D sound field are first reviewed, and a concise derivation of the HREs is then presented by introducing the adiabatic approximation. Rather than pursuing a one-way solution based on the parabolic equation, we explicitly solve for the HRE using a MOR technique, the core of which relies on a modal projection method incorporating PMLs. While valid only for environments invariant along the longitudinal direction, the modal projection method is highly efficient. This method is then extended to address fully 3D scenarios by introducing the concept of an admittance matrix.

2.1. Governing equations

We start with the Helmholtz equation governing 3D underwater acoustic propagation [7]:

$$\frac{\partial^2 p}{\partial x^2} + \frac{\partial^2 p}{\partial y^2} + \rho(z) \frac{\partial}{\partial z} \left(\frac{1}{\rho(z)} \frac{\partial p}{\partial z} \right) + \frac{\omega^2}{c^2(x, y, z)} p = 0, \quad (1)$$

where ω is the angular frequency, and, based on modal decomposition, the sound pressure $p(x, y, z)$ can be written as:

$$p(x, y, z) = \sum_j R_j(x, y) P_j(x, y, z), \quad (2)$$

where j specifies the vertical mode number, $R_j(x, y)$ are the modal coefficients, and the orthogonal, vertical modes $P_j(x, y, z)$ satisfy the local water/seafloor continuity conditions at $z = z_{sf}(x, y)$ and the pressure-release condition at $z = 0$:

$$\begin{cases} P_j(x, y, z) \Big|_{z=0} = 0, \\ \frac{1}{\rho(z)} \frac{dP_j(x, y, z)}{dz} \Big|_{z=z_{sf}^-} = \frac{1}{\rho(z)} \frac{dP_j(x, y, z)}{dz} \Big|_{z=z_{sf}^+}. \end{cases} \quad (3)$$

Substituting Eq. (2) back into Eq. (1) and ensuring the orthogonality of the local vertical mode:

$$\int (\cdot) \frac{P_h(x, y, z)}{\rho(z)} dz, \quad (4)$$

this yields

$$\frac{\partial^2 R_j}{\partial x^2} + \frac{\partial^2 R_j}{\partial y^2} + k_{rj}^2(x, y)R_j + \sum_h A_{h,j}R_h + 2 \sum_h B_{h,j} \frac{\partial R_h}{\partial x} + 2 \sum_h C_{h,j} \frac{\partial R_h}{\partial y} = 0, \quad (5)$$

where $A_{h,j}$, $B_{h,j}$, and $C_{h,j}$ are the coupling matrices, the detailed expressions for which can be found in [7,47]. In the above equation, k_{rj} are the horizontal modal wavenumbers. Dropping the coupling terms gives the adiabatic approximation of the coupled equation in Eq. (5), and the so-called HRE is finally derived:

$$\frac{\partial^2 R_j}{\partial x^2} + \frac{\partial^2 R_j}{\partial y^2} + k_{rj}^2(x, y)R_j = 0. \quad (6)$$

Clearly, the modal coefficients are governed by the uncoupled 2D Helmholtz-type equation, as expressed in Eq. (6). These 2D Helmholtz-type equations, previously examined through ray theory and the parabolic equation, fundamentally depict modal coefficients within the unbounded horizontal domain. The horizontal wavenumber k_{rj} determines the effective index of refraction.

2.2. Model order reduction

We introduce a MOR based on normal mode theory to solve the 2D Helmholtz-type equations in Eq. (6). This involves a transverse modal decomposition of the coefficients $R_j(x, y)$, which is described by:

$$R_j(x, y) = \sum_{n=1}^{\infty} S_j^n(x) \phi_j^n(y), \quad (7)$$

where $\phi_j^n(y)$ represents the transverse eigenfunctions of $R_j(x, y)$ and $S_j^n(x)$ denotes their coefficients. The superscript n indicates the order of the transverse eigenfunctions. In essence, the transverse eigenfunctions of $R_j(x, y)$ span a lower-dimensional, orthogonal space onto which $R_j(x, y)$ are projected. Consequently, the original model, characterized by discretization points along the transverse direction, is reduced to a lower-dimensional model in terms of the transverse eigenfunctions $\phi_j^n(y)$. Typically, the number of discretization points along the transverse direction is much larger than the number of transverse eigenfunctions. Therefore, Eq. (7) is essentially a form of MOR based on normal mode theory. By reducing the model order of the modal coefficients, the 3D sound pressure can be written as a double summation

$$p(x, y, z) = \sum_j \sum_n S_j^n(x) \phi_j^n(y) P_j(x, y, z). \quad (8)$$

However, Eq. (7) is a general normal-mode expression that is usually suitable for a bounded space. For 3D underwater acoustic propagation, the horizontal domain is unbounded. Therefore, the strategy here is to artificially truncate the infinite space along the transverse directions using two PMLs with physical outer boundaries. By doing this, the eigenproblem associated with $\phi_j^n(y)$ can be solved using a method of modal projection. Furthermore, the contribution of branch cuts arising from the infinite space is automatically eliminated by introducing two actual boundaries.

2.3. A modal projection method for longitudinally invariant environments

In this context, we begin by simplifying the problem, assuming longitudinal invariance in the environment. This implies that the waveguide geometries and medium properties (k_{rj}) remain constant along the longitudinal direction. This simplification leads to the separation of variables in Eq. (6), indicating that the transverse eigenfunctions $\phi_j^n(y)$ become uncoupled. Considering a monopole point source as an excitation, the coefficients of the transverse eigenfunctions $S_j^n(x)$ are reduced to be range-independent:

$$S_j^n(x) = \frac{i}{2} \phi_j^n(y_s) \frac{e^{ik_{xj}^n x_s}}{k_{xj}^n}, \quad (9)$$

where k_{xj}^n are the transverse eigenvalues and (x_s, y_s) is the horizontal coordinate of the source.

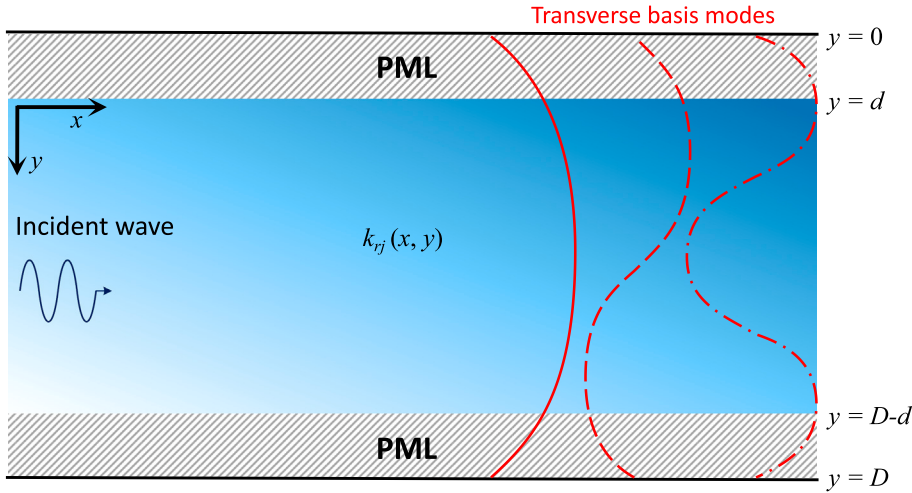


Fig. 2. A schematic of the horizontal computation domain, with its transverse directions truncated by two PMLs. The 2D domain represents the horizontal plane of modal coefficients $R_j(x, y)$, with the medium inhomogeneity characterized by the effective index of refraction $k_{rj}(x, y)$. The transverse basis modes are visualized by the red lines, which are used to span a lower-dimensional projection space for the higher dimensional variables $R_j(x, y)$. (For interpretation of the references to color in this figure legend, the reader is referred to the web version of this article.)

The aforementioned variable separation presupposes the invariance of the waveguide environment along the x -axis, resulting in k_{rj} being solely a function of y . By substituting Eq. (7) back into Eq. (6), the eigenequation for $\phi_j^n(y)$ can be derived:

$$\frac{d^2\phi_j^n}{dy^2} + k_{rj}^2(y)\phi_j^n = k_{xj}^{n,2}\phi_j^n. \quad (10)$$

It is now evident that the longitudinal invariance simplifies the original 2D problem of determining $R_j(x, y)$ into a one-dimensional eigenproblem linked to ϕ_j^n . Consequently, there is potential for a significant enhancement of the computational efficiency. The next step involves solving the eigenproblem through a modal projection method.

We now consider an infinite domain, as illustrated in Fig. 2, where the transverse direction is truncated by two PMLs. We define the outer boundaries of the upper and lower PMLs as $y = 0$ and $y = D$, respectively, and these boundaries are characterized by the Dirichlet conditions. Each PML has a thickness of d . By choosing basis modes that meet the boundary conditions at $y = 0$ and $y = D$, the transverse eigenfunctions $\phi_j^n(y)$ are projected onto a series of transverse basis functions:

$$\begin{cases} \phi_j^n(y) = \sum_{m=1}^N w_j^{m,n} \psi_j^m(y) = \Psi \mathbf{w}^T, \\ \psi_j^m(y) = \sqrt{\frac{2}{D}} \sin \left[\frac{m\pi}{D} y \right]. \end{cases} \quad (11)$$

where ψ_j^m denotes the transverse basis modes within the region bounded by the outer boundaries of the two PMLs, as indicated by the red lines in Fig. 2. The projection coefficients are denoted by $w_j^{m,n}$. The row vectors Ψ and \mathbf{w} represent $1 \times N$ vectors of the transverse basis modes and projection coefficients, respectively. The variables N and the superscript m signify the total number and order of the transverse basis modes, respectively. Multiplying Eq. (10) by Ψ^T and integrating the resulting weighted eigenequation over the interval $0 \leq y \leq D$ gives:

$$\int_0^D \Psi^T \left[\frac{d^2\phi_j^n}{dy^2} + k_{rj}^2(y)\phi_j^n \right] d\hat{y} = k_{xj}^{n,2} \int_0^D \Psi^T \phi_j^n d\hat{y}. \quad (12)$$

where \hat{y} is the complex coordinate stretching induced by the PML, which is mathematically expressed as [39]:

$$\hat{y} = y + \frac{i}{k_{rj}} \int_0^y \sigma(\epsilon) d\epsilon, \quad (13)$$

where $\sigma(\epsilon)$ is the damping function and ϵ is the dimensionless coordinate. For the upper PML, $\epsilon = (d - y)/d$, and for the lower PML, $\epsilon = (y - D + d)/d$. Here, a second-degree polynomial damping function is used, expressed mathematically as $\sigma(\epsilon) = \zeta \epsilon^2$ [48,49], where ζ is a positive real damping coefficient that controls the rate of damping. From Eq. (13), we obtain

$$\begin{aligned} \frac{d}{d\hat{y}} &= \frac{1}{s(y)} \frac{d}{dy}, \\ d\hat{y} &= s(y) dy, \end{aligned} \quad (14)$$

where

$$\begin{aligned} s(y) &= 1, \quad d < y < D - d, \\ s(y) &= 1 + i\sigma(y), \quad \text{otherwise}. \end{aligned} \quad (15)$$

Next, we consider the projection defined by Eq. (11) and substitute Eq. (11) into Eq. (12). After performing integration by parts to reduce the second-order derivatives to first-order derivatives, we obtain the matrix equation

$$[\Gamma + \Pi]\mathbf{W} = k_{xj}^n \mathbf{\Upsilon} \mathbf{W}, \quad (16)$$

where \mathbf{W} is an $N \times N$ transverse projection coefficient matrix, and Γ , Π , and $\mathbf{\Upsilon}$ are

$$\begin{aligned} \Gamma &= \int_0^D -\frac{1}{s(y)} \frac{\partial \Psi^T}{\partial y} \frac{\partial \Psi}{\partial y} dy, \\ \Pi &= \int_0^D k_{rj}^2 s(y) \Psi^T \Psi dy, \\ \mathbf{\Upsilon} &= \int_0^D s(y) \Psi^T \Psi dy. \end{aligned} \quad (17)$$

Analytical expressions can be derived for the integrals containing the derivatives in Γ and the first-order term in $\mathbf{\Upsilon}$. However, Π must be integrated numerically. The numerical scheme follows the Clenshaw–Curtis quadrature rules [40,50,51], which provide excellent convergence using relatively few transverse samplings; generally, five points per period of the basis modes are sufficient to ensure good convergence [40]. A generalized matrix eigenvalue problem can be obtained by rearranging Eq. (16) as follows:

$$\mathbf{K}\mathbf{W} = k_{xj}^n \mathbf{W}, \quad (18)$$

with $\mathbf{K} = \mathbf{\Upsilon}^{-1}(\Gamma + \Pi)$. The generalized matrix eigenvalue problem described above can be readily solved using the built-in MATLAB (MathWorks, Natick, MA, USA) function ‘eig(\mathbf{K})’ once \mathbf{K} is calculated and assembled. It is noteworthy that k_{rj} must be pre-calculated and treated as a known refractive index in a set of HREs given in Eq. (6).

After solving the above eigenvalue problem, the eigenvalues must be sorted in order. Their eigenvectors represent the projection coefficients. The transverse eigenfunctions $\phi_j^n(y)$ are reconstructed using the transverse projection defined in Eq. (11), and the modal coefficients $R_j(x, y)$ can be calculated using Eqs. (7) and (9). It is important to highlight that projecting ϕ_j^n onto the space defined by ψ_j^m enables the conversion of the original eigenproblem linked with k_{xj}^n into a generalized matrix eigenproblem, simplifying its solution through eigenvalue decomposition of \mathbf{K} .

The dependence on k_{rj} is evident in the generalized matrix eigenvalue problem, where the sub-matrix block, computed using Eq. (17), is explicitly a function of k_{rj} . Essentially, the variable-separated wave equation given by Eq. (10) generates distinct generalized matrix eigenvalue problems for various horizontal wavenumbers k_{rj} . As a result, this process determines different $R_j(x, y)$ corresponding to k_{rj} for different orders of vertical modes. Subsequently, the computation of the 3D horizontal sound field is performed using Eq. (2) once all orders of $R_j(x, y)$ are obtained.

The preceding derivation highlights that the proposed MOR technique, coupled with the assumption of longitudinal invariance, facilitates the simultaneous computation of $R_j(x, y)$ for various x and y coordinates once the eigenproblem of the transverse eigenfunctions $\phi_j^n(y)$ in Eq. (10) is resolved. This characteristic fundamentally bypasses the evolutionary procedure typically associated with the x -direction in the standard parabolic equation. Consequently, the proposed MOR technique proves highly efficient when the environment exhibits invariance along the longitudinal direction. Despite the restriction on range independence along the longitudinal direction, we expand the MOR technique to address fully 3D scenarios in the following section.

2.4. An admittance matrix for fully three-dimensional environments

In reality, the underwater environment is more complex than the longitudinally invariant scenario discussed in the preceding section and can exhibit various 3D characteristics. To handle fully 3D environments effectively, we enhance the MOR method by introducing an admittance matrix. This matrix essentially aligns with the Dirichlet-to-Neumann (DtN) operator, signifying the radiation condition in the transverse modal domain. A Riccati equation typically governs the admittance matrix, providing an efficient and stable numerical solution to the fully 2D Helmholtz-type equation in Eq. (6).

The starting point is to write Eq. (6) as a first-order evolution equation along the longitudinal direction x [42]:

$$\frac{\partial}{\partial x} \begin{bmatrix} R_j \\ R'_j \end{bmatrix} = \begin{bmatrix} 0 & 1 \\ -(\partial_y^2 + k_{rj}^2) & 0 \end{bmatrix} \begin{bmatrix} R_j \\ R'_j \end{bmatrix}, \quad (19)$$

where $\partial_y^2 = \frac{\partial^2}{\partial y^2}$ and R'_j denotes the partial derivative of R_j along x . The transverse basis modes are then used to project R_j and R'_j directly, yielding:

$$\begin{cases} R_j(x, y) = \sum_{m=1}^N a_j^m(x) \psi_j^m(y), \\ R'_j(x, y) = \sum_{m=1}^N b_j^m(x) \psi_j^m(y), \end{cases} \quad (20)$$

where a_j^m and b_j^m represent the coefficients of the m th-order transverse basis mode for R_j and R'_j , respectively.

Notably, given the range independence of the boundaries at $y = 0$ and $y = D$, the transverse basis modes $\psi_j^m(y)$ in Eq. (20) are identical to those in Eq. (11), and they do not depend on x . Expressing Eq. (20) in matrix form and subsequently substituting it into Eq. (19) results in

$$\frac{\partial}{\partial x} \begin{bmatrix} \mathbf{a}_j(x)^T \\ \mathbf{b}_j(x)^T \end{bmatrix} = \begin{bmatrix} \mathbf{0} & \mathbf{I} \\ -\mathbf{K} & \mathbf{0} \end{bmatrix} \begin{bmatrix} \mathbf{a}_j(x)^T \\ \mathbf{b}_j(x)^T \end{bmatrix}, \quad (21)$$

where the matrix \mathbf{K} is the same as that in Eq. (18).

Considering numerical stability, we cannot directly treat the coupled equations for transverse basis modes in Eq. (21) as an initial problem. Instead, we introduce an admittance matrix represented as

$$\mathbf{b}_j = \mathbf{Y}_j \mathbf{a}_j. \quad (22)$$

One can then obtain the governing Riccati equation:

$$\frac{\partial \mathbf{Y}_j}{\partial x} = -\mathbf{K} - \mathbf{Y}_j^2. \quad (23)$$

The solution to Eq. (21) is computed through a two-step procedure: (a) Eq. (23) is numerically integrated from $x = x_L$, where the longitudinal range is truncated, using an initial value of $\mathbf{Y}_j(x_L) = i\sqrt{\mathbf{K}}$, to $x = x_0$, where the source condition is imposed. (b) The coupled coefficients $\mathbf{a}_j(x)$ of transverse basis modes are calculated by providing an initial source condition at $x = x_0$:

$$\frac{\partial \mathbf{a}_j}{\partial x} = \mathbf{Y}_j \mathbf{a}_j. \quad (24)$$

Here, we employ the Magnus–Möbius scheme [45,46] to numerically compute Eqs. (23) and (24). The form of these two equations is similar to the so-called invariant embedding equations [52–54]. For clarity, we provide details of the second-order Magnus scheme below, which is consistently applied in this article. Further details regarding higher-order Magnus schemes can be found in the work of Iserles et al. [55]. We assume a uniform discretization of the longitudinal range with a step size of $\Delta x = x_1 - x_0 > 0$. Utilizing the second-order Magnus scheme, Eq. (21) can be expressed in a numerical discretized form:

$$\begin{bmatrix} \mathbf{a}_j(x - \Delta x)^T \\ \mathbf{b}_j(x - \Delta x)^T \end{bmatrix} = e^{-\Delta x \mathbf{H}[x - (\Delta x/2)]} \begin{bmatrix} \mathbf{a}_j(x)^T \\ \mathbf{b}_j(x)^T \end{bmatrix}, \quad (25)$$

with

$$\mathbf{H} = \begin{bmatrix} \mathbf{0} & \mathbf{I} \\ -\mathbf{K} & \mathbf{0} \end{bmatrix}. \quad (26)$$

The exponential propagator is decomposed into

$$e^{-\Delta x \mathbf{H}[x - (\Delta x/2)]} = \begin{bmatrix} \mathbf{E}_1 & \mathbf{E}_2 \\ \mathbf{E}_3 & \mathbf{E}_4 \end{bmatrix}. \quad (27)$$

The Riccati equation for \mathbf{Y}_j is eventually solved following the Magnus scheme, yielding:

$$\mathbf{Y}_j(x - \Delta x) = [\mathbf{E}_3 + \mathbf{E}_4 \mathbf{Y}_j(x)][\mathbf{E}_1 + \mathbf{E}_2 \mathbf{Y}_j(x)]^{-1}, \quad (28)$$

and the range-dependent, transverse basis modal coefficients $\mathbf{a}_j(x)$ can be solved using a forward evolutionary procedure:

$$\mathbf{a}_j(x) = \mathbf{M}_j(x)^{-1} \mathbf{a}_j(x - \Delta x), \quad (29)$$

with $\mathbf{M}_j(x) = \mathbf{E}_1 + \mathbf{E}_2 \mathbf{Y}_j(x)$.

Following the computation of the transverse basis modal coefficients $\mathbf{a}_j(x)$, $R_j(x, y)$ can be determined using Eq. (20) with an initial value of $\mathbf{a}_0(x) = -[\exp(i\sqrt{\mathbf{K}}x_s)/2i\sqrt{\mathbf{K}}]\Psi(y_s)$. As the coupled equations in Eq. (21) are solved through an evolutionary procedure, the risk of numerical overflow is mitigated. Fig. 3 provides a visual representation of the evolutionary procedure. Notably, at each step of the evolutionary procedure, only the matrix $-\mathbf{K}$ requires recomputation and updating. This is attributed to the independence of the outer boundaries of the artificially truncated domain. Consequently, only the product of $\mathbf{E}_1 + \mathbf{E}_2 \mathbf{Y}_j(x)$ (or its inverse) must be stored throughout the entire evolutionary procedure, allowing the overwriting of other matrices. This practice conserves RAM and enhances computational efficiency.

Furthermore, the admittance matrix achieves superior convergence to the classical step-wise approximation. In the Magnus scheme, it is typically advised to keep the step size, represented by Δx , smaller than half the wavelength (λ). This guideline is effective when utilizing the admittance matrix to solve sound propagation in waveguides with varying cross-sections [56]. However, in our study, the outer boundary of the PMLs remains constant along the x -axis. Consequently, the sole factor causing scattering is the inhomogeneity in $k_{rj}(x, y)$, which can be viewed as a slowly varying function with respect to x . Hence, our proposed model can perform admirably even with a coarser grid. We provide comparisons of the sound field computed across different grids along the x -axis in Section 3.3.1, affirming this characteristic of the proposed MOR technique.

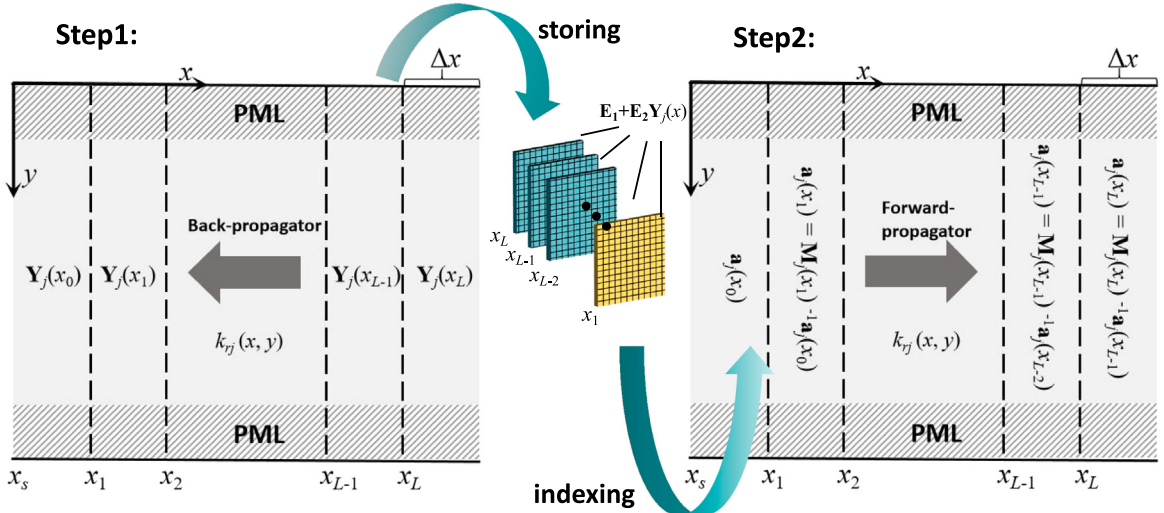


Fig. 3. A flow chart of the evolutionary Magnus scheme for solving the coupled transverse modal coefficients $\mathbf{a}_j(x)$ when the range dependence of k_{rj} is introduced. This first involves a back-propagator step to compute the admittance matrices with an initial condition of $\mathbf{Y}_j(x_L) = i\sqrt{\mathbf{K}}$, starting from x_L to x_0 where the source condition is imposed. During this process, the product of $\mathbf{E}_1 + \mathbf{E}_2 \mathbf{Y}_j(x)$ is stored at each evolutionary step. The second step uses the stored matrices to forward propagate the coupled transverse modal coefficients $\mathbf{a}_j(x)$ from x_1 to the end of the 2D computation domain at x_L , such that the $\mathbf{a}_j(x)$ at each x are obtained.

3. Numerical simulations

This section presents the results of the numerical simulations. Four test cases are divided into two groups, each intended to validate the proposed MOR technique for either longitudinally invariant environments or fully three-dimensional environments. Initially, the Acoustical Society of America (ASA) benchmark wedge [10] is simulated with longitudinal invariance, where horizontal refraction dominates. This scenario serves as a suitable benchmark for evaluating the proposed MOR technique's efficacy in solving HREs without modal coupling. The second example involves the infinite cosine hill, where both modal coupling and horizontal refraction are significant, elucidating how the proposed model performs when the adiabatic assumption is violated. Transitioning to fully three-dimensional environments, two cases are examined. Firstly, the corrugated seafloor case demonstrates the proposed model's effectiveness in environments where modal coupling is weak. Subsequently, the sandbar scenario, incorporating realistic topography data, explores the model's applicability in environments where modal coupling may occur locally.

The simulations were implemented using MATLAB installed on a laptop with an Intel Core i9-13900K CPU (Intel, Santa Clara, CA, USA) and 128 GB RAM. A point source with unit amplitude was considered in all simulations, which were conducted for a two-layer fluid shallow-water environment with a constant water sound speed of 1500 m/s. Consequently, the local vertical modes $P_j(x, y, z)$ for the Pekris waveguide could be computed analytically, and their corresponding horizontal wavenumbers were determined using a root finder based on Newton-Raphson iteration [57]. For detailed information on the root finder, please refer to Appendix A.1. It is important to note that when dealing with refractive water, alternative numerical tools are required to solve waterborne modes and their eigenvalues, such as KRAKEN [58] and ORCA [59]. Although all the simulations assumed an iso-velocity water column, the proposed model can adapt to sound speed inhomogeneity in both the vertical and horizontal directions once the local vertical modes and their horizontal wavenumbers are established for refractive water. It is imperative to consider the presence of vertical leaky modes in all simulations, as they make a substantial contribution to the near field. To enhance accuracy across all ranges, we incorporate these vertical leaky modes into the wave solution. Vertical leaky modes typically refer to those with high mode orders, resulting in high attenuation and exponential decay within the water column as they escape into the sediment. Thus, for the purpose of this study, vertical leaky modes are operationally defined as those propagating over short distances with mode orders higher than those capable of long-range propagation.

In these simulations, computational efficiency and accuracy should be guaranteed by setting appropriate transverse basis mode number N , PML damping coefficient ζ , and PML thickness d . Selecting an appropriate thickness for the PML is often highly contingent on the specific problem at hand and is not always straightforward. Ideally, the PML should possess adequate thickness to facilitate significant coordinate stretching, ensuring exponential decay of the wave solution within it. While increasing PML thickness undoubtedly enhances attenuation of outgoing waves, it invariably escalates computational costs. Striking a balance between accuracy and efficiency, a PML thickness of 5λ proved effective in our simulations and was consequently adopted for subsequent analyses. The following part first discuss the parameter selection for the proposed MOR technique. The suggested parameters are then used for presenting all the numerical simulations throughout this article.

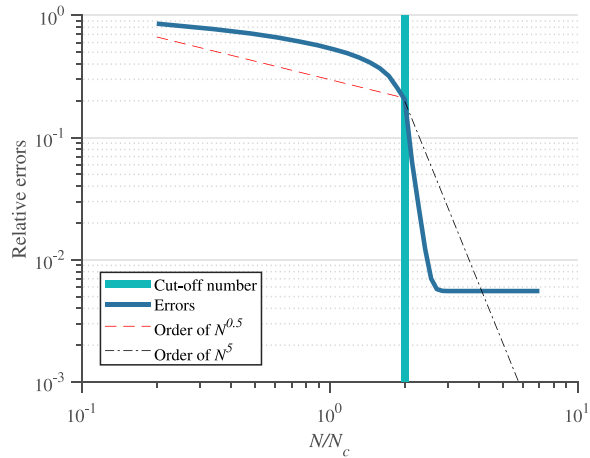


Fig. 4. Relative error curve as a function of N/N_c at 125 Hz. The results are shown for the Pekeris waveguide.

3.1. Parameter selection

The subsequent analysis addresses parameter selection for the proposed MOR technique. This entails examining error convergence concerning an analytical solution. The chosen analytical solution is the sound field in a Pekeris waveguide:

$$p_{\text{anay}}(x, y, z) = \sum_j L_j^{-2} \sin(k_{zj} z_s) \sin(k_{zj} z) H_0^1(k_{rj} |\mathbf{r} - \mathbf{r}_s|), \quad (30)$$

where $k_{zj} = \sqrt{k^2 - k_{rj}^2}$, $\mathbf{r}_s = (x_s, y_s)$ denotes the source's horizontal position vector, $\mathbf{r} = (x, y)$ signifies the horizontal position vector of field points, and L_j^{-2} are the normalized coefficients whose expression can be found in [Appendix A.1](#). The analysis frequency is 125 Hz, corresponding to the upper frequency limit of the numerical simulations in this study. The water depth is set at 200 m. Seabed parameters are adopted from Case 1 in [Table 1](#). A horizontal domain of 20 km \times 4 km size is utilized for computation, with a receiver depth of 150 m. The source is positioned at (0 km, 2 km, 100 m). To assess the convergence of the proposed MOR technique, we introduce relative errors:

$$\text{Relative Errors} = \frac{\int |p_{\text{anay}} - p|^2 dx dy}{\int |p_{\text{anay}}|^2 dx dy}, \quad (31)$$

where $dx = \Delta x = \lambda/5$ and $dy = \Delta y = \lambda/5$. In the subsequent discussion on parameter selection, default values of N , ζ , and d are $3Df/c_{pj}$, 1, and 5λ , respectively, unless specified otherwise. Here, c_{pj} represents the modal phase velocity of the j th vertical mode.

3.1.1. Total number of transverse basis modes

[Fig. 4](#) illustrates the relative errors plotted against the ratio of N to $N_c = Df/c_{pj}$. The relative errors exhibit a gradual decrease following $1/N^{0.5}$ when $N < 2N_c$, beyond which they diminish more rapidly following about $1/N^5$. Once $N > 2.5N_c$, the relative errors converge to approximately 0.6%. In the modal projection method, the modal coefficients are determined by truncating the horizontal infinite space with two PMLs, encompassing both the continuous spectrum and the discrete spectrum. The latter comprises transverse basis modes with mode orders less than $n < 2N_c$ for a bounded space [\[7\]](#). However, when dealing with the truncated infinite space, the discrete spectrum alone is insufficient, necessitating the inclusion of transverse leaky modes, which contribute solely to the near field or escape into the infinite space, to accurately approximate the continuous spectrum. Notably, for a bounded space, high-order modes, representing the so-called evanescent modes, may be excited after $n > 2N_c$, exhibiting attenuating behavior that aligns with the absorption of reflections from outer boundaries (leaky energy). Considering the escalating numerical cost with increasing N , and observing that $N = 3N_c$ yields satisfactory accuracy with errors marginally exceeding 1%, we adopt this value for subsequent simulations.

3.1.2. PML damping coefficient

To ascertain the optimal damping coefficient ζ , [Fig. 5](#) illustrates the relative errors plotted against ζ . Additionally, the error curve at 25 Hz is provided to illustrate the attenuation rate's frequency dependency in the PMLs, which is mitigated by incorporating the horizontal wavenumber k_{rj} in Eq. [\(13\)](#). Initially, errors decrease with increasing ζ , aligning with the polynomial damping functions' capability to mitigate spurious reflections from the PMLs' outer boundary through enlarging the damping coefficients. Once reaching their minima, errors stabilize before gradually increasing. This increase in errors can be attributed to excessive stretching induced by overlarge damping coefficients. Both error curves at the two frequencies reach their minima within the ζ range of 0.5 to 5, affirming that considering k_{rj} in Eq. [\(13\)](#) effectively mitigates the frequency dependency of the attenuation rate in PML. This analysis suggests that robust results can be achieved with $\zeta = 1$, and we adopt this value for subsequent simulations.

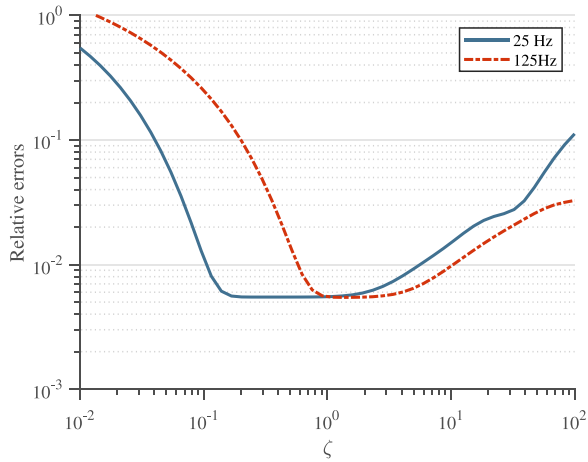


Fig. 5. Relative error curve as a function of ζ at 25 Hz and 125 Hz. The results are shown for the Pekeris waveguide.

Table 1
Parameters of the longitudinally invariant shallow-water environment in the simulations.

Parameter	Case 1: ASA wedge	Case 2: Infinite cosine hill
Computational frequency	25 Hz	100 Hz
Computational domain size	25 km \times 8 km \times 400 m	20 km \times 8 km \times 60 m
Seabed sound speed	1700 m/s	1767 m/s
Seabed sound attenuation	0.5 dB/ λ	0.75 dB/ λ
Seabed density	1500 kg/m ³	1845 kg/m ³
Numbers of vertical modes	8	6
Computation time	1.2 s	14 s

3.2. Longitudinally invariant environments

3.2.1. Case 1: ASA wedge

The first case is the ASA benchmark wedge, whose topography is described by:

$$z_{sf}(x, y) = 200 + 0.05(y - y_s). \quad (32)$$

The seabed parameters are provided in [Table 1](#). The seabed slope of the ASA benchmark wedge measures approximately 2.86°, resulting in noticeable horizontal refraction along the x -axis. Consequently, the ASA benchmark wedge is commonly utilized to evaluate 3D propagation effects, making it an appropriate case for benchmarking the proposed MOR technique, which neglects mode interactions. The point source is positioned at (0 km, 4 km, 100 m) with a frequency of 25 Hz. Eight vertical modes are considered in the computation. [Fig. 6](#) provides a schematic of the simulation setup.

[Fig. 7](#) illustrates the sound propagation in the horizontal plane at $z = 30$ m and shows noticeable horizontal refraction along the x -axis. In addition, [Fig. 8](#) shows the coefficients of the first five vertical modes. Higher modes exhibit more significant horizontal refraction, a phenomenon consistent with the observations summarized by Jensen et al. [7]. With each interaction with the seabed, acoustic rays are deflected slightly away from the apex, forming an energy path that curves upslope and ultimately propagates downslope. Steeper rays, corresponding to higher modes, undergo more bottom reflections and are turned around faster than shallow-angle rays, which represent lower-order modes.

To quantitatively validate the proposed MOR technique, the transmission loss (TL) is compared with that computed by the state-of-the-art wide-angle mode parabolic equation [22] and a longitudinally invariant finite element model [1]. [Fig. 9](#) shows excellent agreement with the other two models for the TL plotted as a function of x along $y = y_s$ at a receiver depth of 30 m, thereby validating the proposed model for 3D propagation effects in coastal wedges. It is worth mentioning that the average running time for the proposed MOR is about 1.2 s, significantly faster than the 1 h and 30 min taken by the longitudinally invariant finite element model. Even when compared with the wide-angle mode parabolic equation, the proposed MOR model is still over a hundred times faster. This demonstrates that the proposed model is highly efficient for sound propagation in longitudinally invariant environments.

3.2.2. Case 2: Infinite cosine hill

The second case featuring longitudinal invariance is the infinite cosine hill, depicted in [Fig. 10](#). Compared to the previous case, the infinite cosine hill can induce both strong horizontal refraction and mode coupling, making it suitable for studying mode interactions

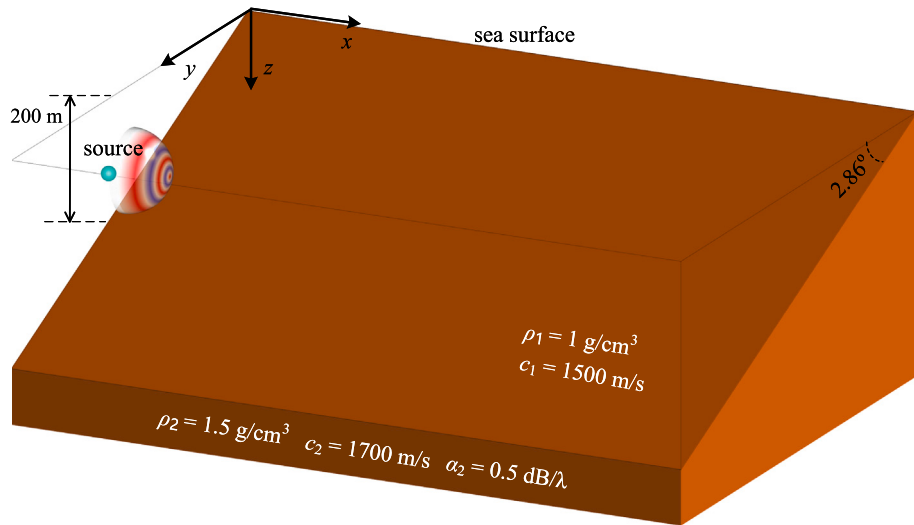


Fig. 6. A schematic of the simulation setup for the ASA benchmark wedge, with the y -axis aligned along the bottom slope.

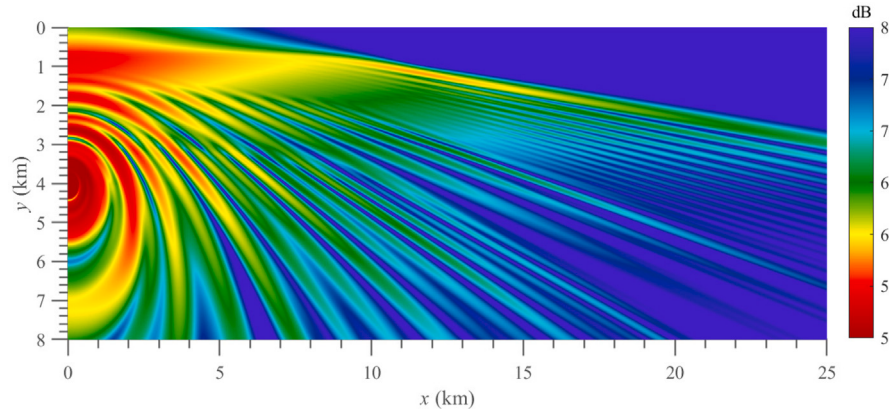


Fig. 7. TL contours in the coastal wedge with a receiver depth of $z = 30 \text{ m}$ at 25 Hz.

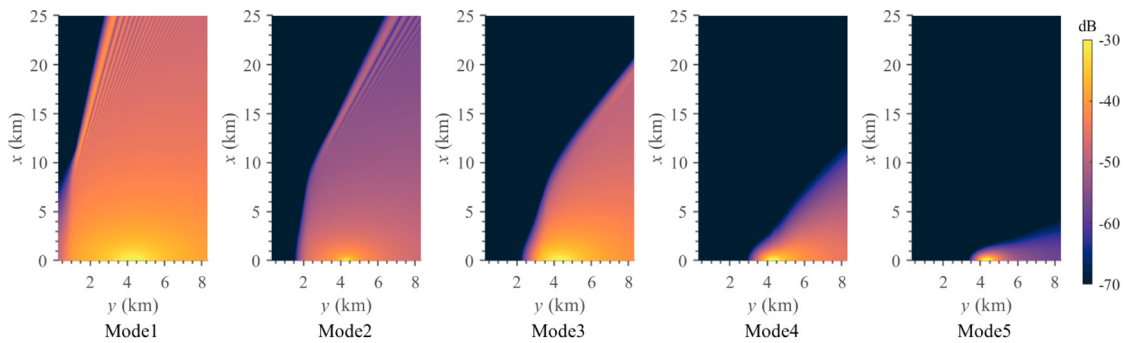


Fig. 8. Modal coefficients of the first five vertical modes in the $z = 30 \text{ m}$ horizontal plane at 25 Hz. The results are shown for the coastal wedge case.

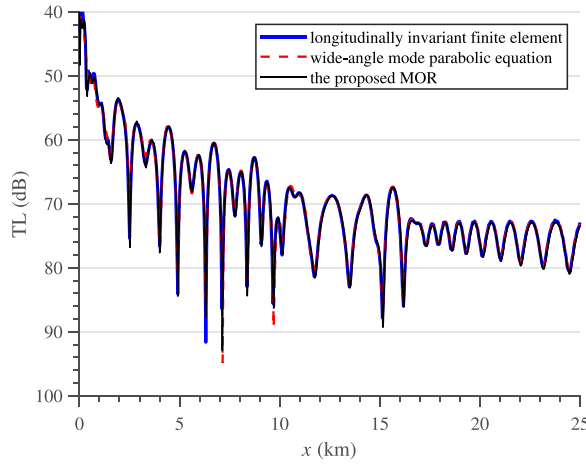


Fig. 9. The TL compared with those from the wide-angle mode parabolic equation (the dashed red line) and longitudinally invariant finite element models (the solid blue line) in the $y = y_s$ plane at a receiver depth of $z = 30$ m. The results are shown for the coastal wedge case. (For interpretation of the references to color in this figure legend, the reader is referred to the web version of this article.)

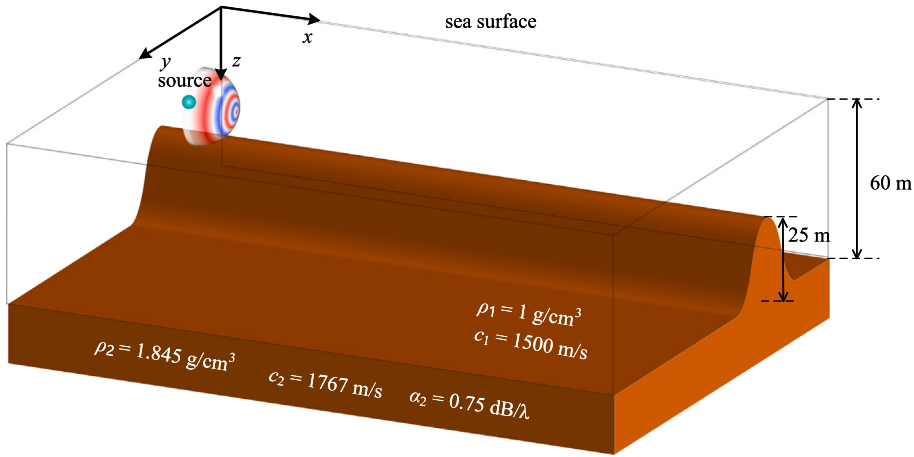


Fig. 10. A schematic of the simulation setup in the case of a cosine hill.

and evaluating the proposed model's suitability. In this case, the cosine hill is described by:

$$z_{sf}(x, y) = \begin{cases} 47.5 - 12.5 \cos \frac{2\pi y}{500}, & 2750 < y - y_s < 3250, \\ 60, & \text{otherwise.} \end{cases} \quad (33)$$

Table 1 summarizes the seabed parameters for this case. The source position is (0 km, 2 km, 20 m), and the source frequency is 100 Hz, at which four trapped modes plus two vertical leaky modes are taken into account. **Fig. 11** compares the results obtained using the proposed MOR technique and the longitudinally invariant finite element model in the $z = 20$ m plane, revealing visible differences when y exceeds 5 km. In this region, the finite element model shows apparent fluctuations in its interference pattern due to mode coupling effects, whereas the proposed model predicts relatively smooth results. Nevertheless, both models demonstrate consistent overall energy distributions. Specifically, the horizontal refraction by the infinite hill beyond x exceeding 12 km is accurately captured by both models.

Fig. 12 presents the coefficients of the first five vertical modes at a receiver depth of 20 m. Modes 2 and 3 demonstrate significant horizontal refraction by the infinite cosine hill, resulting in a shadow zone over the hill beyond $y > 5$ km and $x > 11$ km. In the same region where the shadow zone occurs, mode 1 shows an apparent acoustic energy distribution, contributing to the horizontal diffraction zone observed in the sound field depicted in **Fig. 11**. Additionally, mode 4 is completely cut off by the cosine hill and cannot propagate beyond $y > 5$ km.

Fig. 13 compares the TL along the $y = 4$ km and $y = 7$ km axes at a receiver depth of 20 m. At $y = 7$ km, the proposed model generally underestimates the TL over short ranges but aligns well with the longitudinally invariant finite element model in terms of its overall trend. Specifically, for regions where the horizontal refraction is significant ($y = 4$ km axis), the proposed model yields

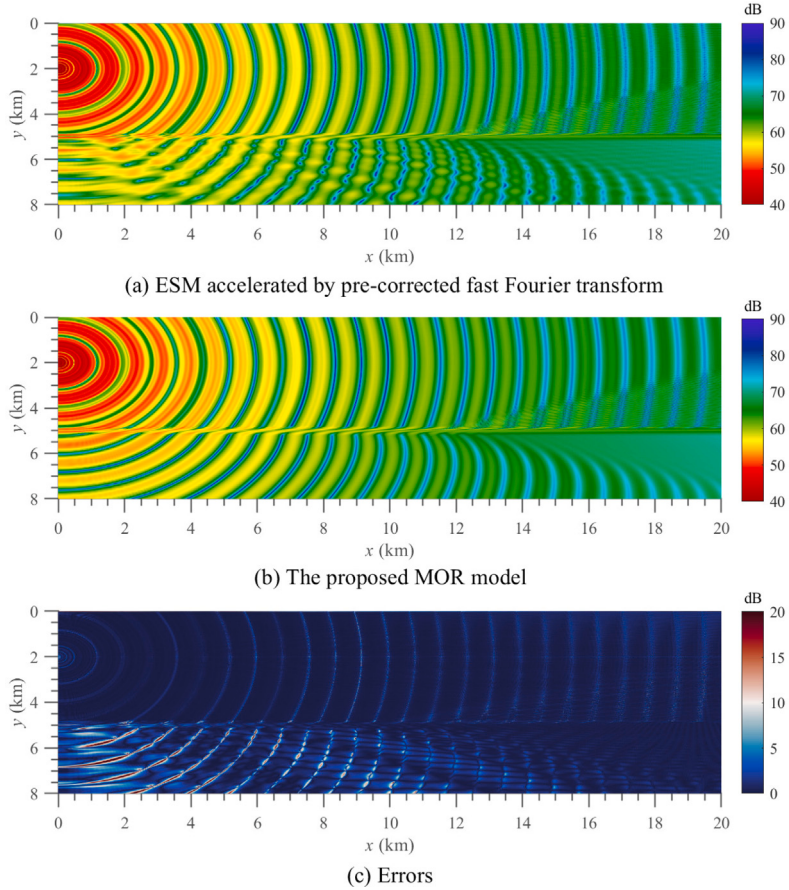


Fig. 11. The TL contours in the ocean overlaying the infinite cosine hill with a receiver depth of $z = 20$ m at 100 Hz, calculated using the longitudinally invariant finite element model (a) and the proposed method (b).

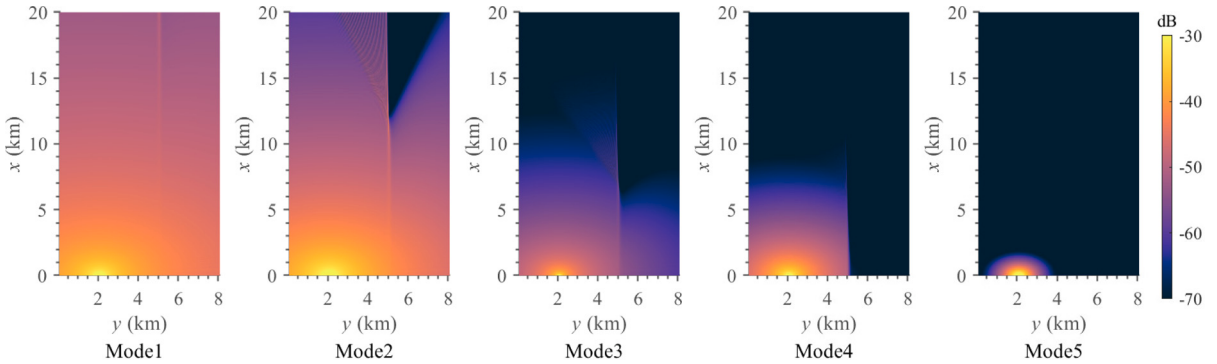


Fig. 12. Modal coefficients the first five vertical modes in the $z = 20$ m horizontal plane at 100 Hz. The results are given for the infinite cosine hill case.

nearly identical results to the finite element model. The errors between the two models, depicted at the bottom of Fig. 11, align with this observation, revealing significant discrepancies of up to 10 dB in regions across the hill and where troughs in the sound field are evident. This suggests that the proposed method is applicable across various underwater scenarios, especially when the mode coupling effect is not the predominant factor influencing sound propagation.

The computation time for this case is approximately 14 s, longer than the previous case. This increase is due to the higher frequency and vertical mode numbers. Nevertheless, it remains acceptable and sufficiently fast for tackling large-scale 3D problems. It is worth noting that the computation time for the longitudinally invariant finite element model in this case, involving the evaluation of the cosine transform along the out-of-plane wavenumbers with 3072 points, is about 8 h and 30 min.

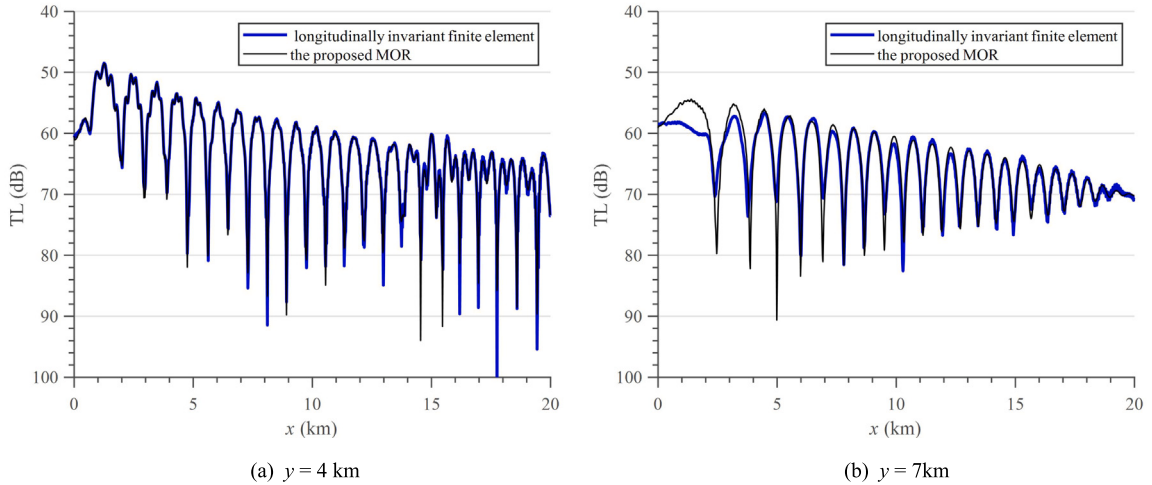


Fig. 13. A TL comparison with the longitudinally invariant finite element model (the solid blue line) in the $y = 4 \text{ km}$ (a) and $y = 7 \text{ km}$ (b) planes at a receiver depth of $z = 20 \text{ m}$. The results are given for the infinite cosine hill case. (For interpretation of the references to color in this figure legend, the reader is referred to the web version of this article.)

Table 2
Parameters of the fully 3D shallow-water environments in the simulations.

Parameter	Case 1: Corrugated seabed	Case 2: Realistic sandbar
Computational frequency	50 Hz	125 Hz
Computational domain size	$8 \text{ km} \times 8 \text{ km} \times 150 \text{ m}$	$4 \text{ km} \times 3 \text{ km} \times 150 \text{ m}$
Seabed sound speed	2000 m/s	1700 m/s
Seabed sound attenuation	$0.0 \text{ dB}/\lambda$	$0.5 \text{ dB}/\lambda$
Seabed density	2000 kg/m^3	1500 kg/m^3
Numbers of vertical modes	6	10
Computation time	18 min	37 min

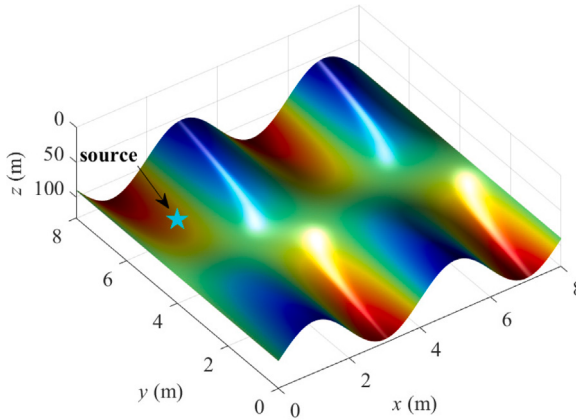


Fig. 14. A schematic of the simulation setup for a corrugated seabed.

3.3. Fully three-dimensional environments

3.3.1. Case 1: Corrugated seabed

In this section, we consider fully 3D underwater environments. The first example illustrates shallow water overlaying a corrugated seabed described by:

$$z_{sf}(x, y) = 90 + \sin \frac{2\pi x}{4000} \tan 0.5^\circ (y - y_s). \quad (34)$$

Table 2 summarizes the corresponding seabed parameters. The source position is (0 km, 4 km, 10 m), with a frequency of 50 Hz. The simulation configuration is depicted in **Fig. 14**. Under this excitation, four vertical modes act as propagating modes. We include

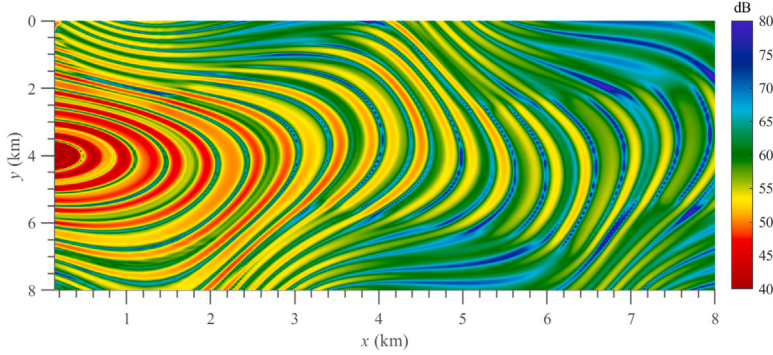


Fig. 15. TL contours in the ocean overlaying the corrugated seafloor. The results are given in the horizontal plane at $z = 10$ m at 50 Hz and calculated using the proposed method.

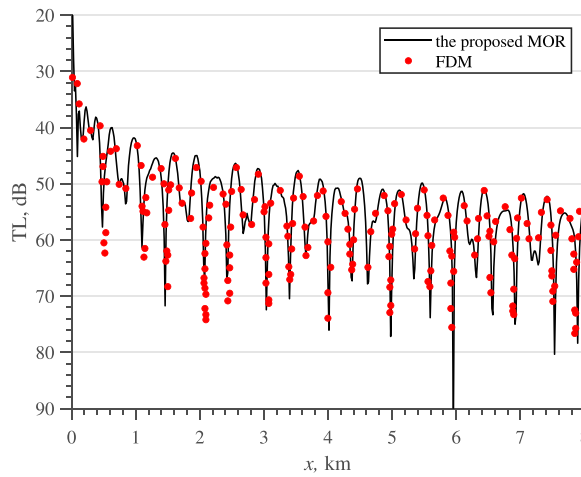


Fig. 16. A comparison of the TL with the full-wave FDM (the solid red circles) in the $y = y_s$ plane at a receiver depth of $z = 10$ m. This is a reproduction of Fig. 15 from Liu et al. [4]. The results are given for the corrugated seabed case.

two additional vertical leaky modes in the computation to achieve convergent results. Sound propagation over the corrugated seabed is primarily influenced by horizontal refraction, with relatively weak mode coupling effects. These aspects will be further discussed in the subsequent analysis by comparison with a full-wave FDM [4]. The step size Δx is set to be a default value of λ unless specified.

Fig. 15 reproduces the TL contours given by Liu et al. [4] using the proposed model in the horizontal plane at $z = 10$ m. Overall, the TL predicted by the proposed model closely approximates the full-wave FDM result. The latter exhibits slightly oscillatory contours of TL in the deep region due to weak mode coupling effects, which are absent in the current model. However, the sound propagation is primarily influenced by horizontal refraction from the corrugated seabed rather than modal interactions. The proposed model demonstrates promising results under such fully 3D circumstances. This is further supported by TL comparisons with the full-wave FDM along the $y = y_s$ axis at a receiver depth of 10 m (see Fig. 16), with root mean square errors barely exceeding 1 dB.

Next, we compare the sound field computed using different grids. Four discretization schemes are considered: $\Delta x = 2\lambda$, $\Delta x = \lambda$, $\Delta x = \lambda/2$, and $\Delta x = \lambda/4$, respectively. The TLs along $y = 2$ km are provided in this case, as shown in Fig. 17. Even at a very coarse grid with $\Delta x = 2\lambda$, one can indeed observe that the TL predicted by our method closely matches the result obtained with the finest grid. This highlights another advantageous aspect of our technique: it enables efficient solutions on a coarser grid without compromising accuracy. To prevent the occurrence of unconvvergent solutions in extreme scenarios, we recommend $\Delta x = \lambda$ for optimal balance between accuracy and efficiency.

To analyze the sound propagation further, Fig. 18 illustrates the coefficients of the first five vertical modes. It is evident that the first three modes are minimally affected by the topography, while mode 4 exhibits significant horizontal refraction due to the corrugated seabed. Although mode 5 also experiences refraction, it decays exponentially with range owing to its leaky characteristics. This analysis suggests that, in this case, mode 4 dominates the 3D propagation effect. Notably, the current analysis does not consider mode coupling effects, which typically involve energy transfer between low- and high-order modes. For instance, the oscillatory contour observed in the deep region may result from the emergence of high-order modes, where energy is transferred from low-order modes as sound propagates from shallow to deep water. The computation time for this case is 18 min. While slower than longitudinally invariant cases, this duration remains acceptable for large-scale 3D underwater acoustic simulations.

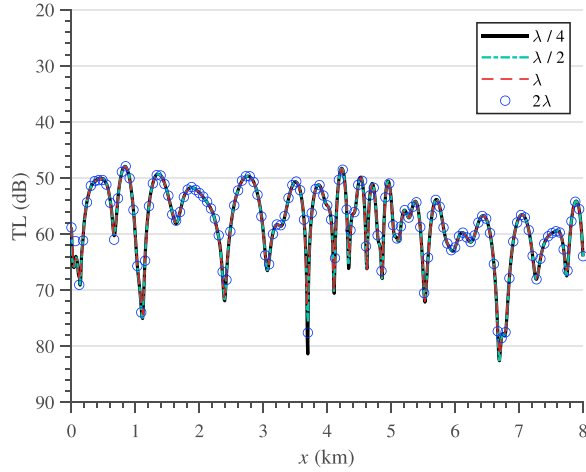


Fig. 17. A comparison of the TL along $y = 2$ km, computed using different grids along the x-axis. The results are given for the corrugated seafloor case.

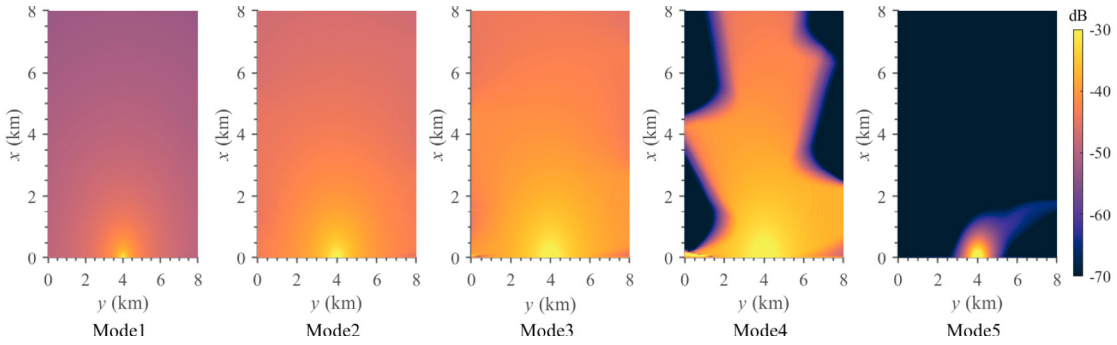


Fig. 18. Modal coefficients of the first five vertical modes in the $z = 10$ m horizontal plane at 50 Hz. The results are given for the corrugated seabed case.

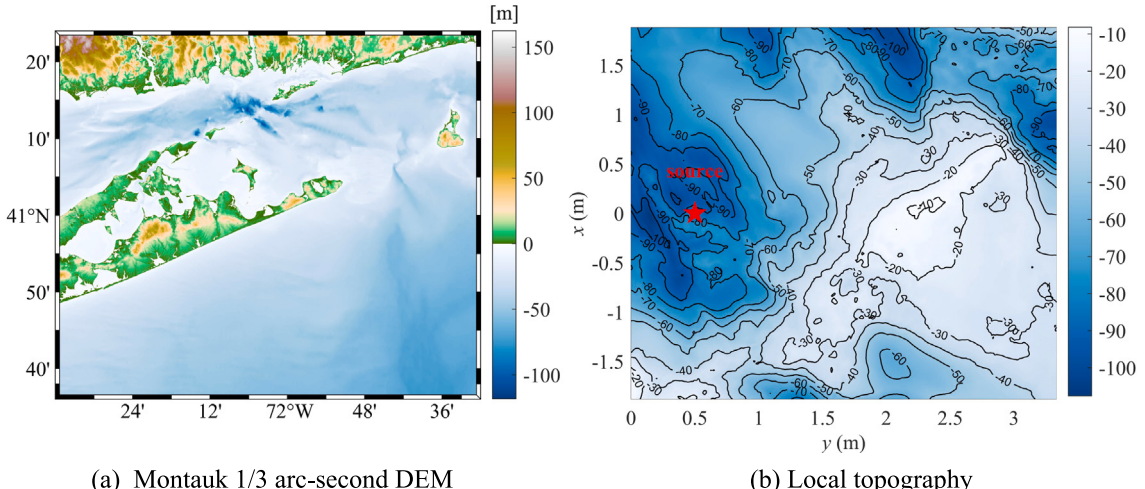


Fig. 19. (a) The shallow water environment of Long Island Sound, with a bathymetric model constructed using the Montauk, New York 1/3 arcsecond digital elevation model from the NOAA dataset. (b) The local topography used in the underwater sound propagation simulations; the red star indicates the horizontal position of the sound source.

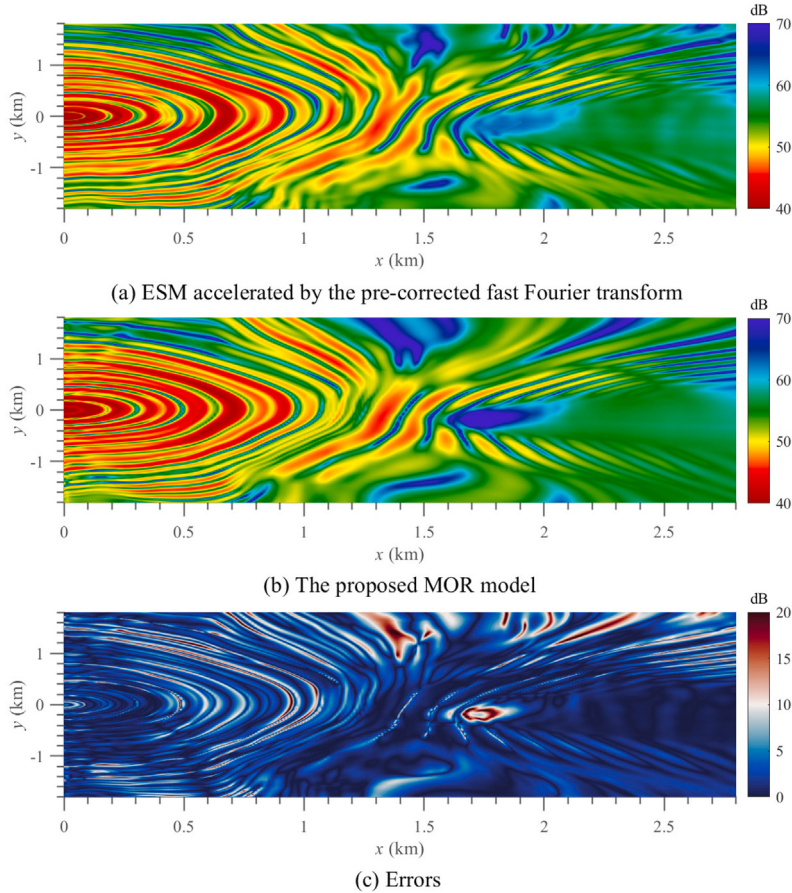


Fig. 20. TL contours in the ocean overlaying the local topography given in Fig. 19(b), with a receiver depth of 20 m. The upper and middle rows show the results computed by the full-wave PFFT-ESM and the proposed model, respectively. The lower row give the errors between these two models.

3.3.2. Case 2: Realistic sandbar

To further demonstrate the capability of the proposed method to model sound propagation associated with intricate topographies, we present a simulation using the bathymetry data of Long Island Sound on the eastern coast of the United States [60] as an illustrative example. The topography in this region exhibits significant variability and strong range dependence, which can potentially induce notable 3D effects even at short distances. As shown in Fig. 19(a), we derived the bathymetric dataset from the National Oceanic and Atmospheric Administration (NOAA) dataset [61]. More specifically, as shown in Fig. 19(b), we extracted a localized topography for the subsequent simulations. The selected topography is from 41.24°N to 41.21°N in latitude and from 72.1°W to 72.04°W in longitude, resulting in an actual area of 3.33 km by 3.76 km. In our simulation setup, the sound source is positioned at coordinates (0 m, 500 m, -60 m), as marked in Fig. 19(b). Table 2 summarizes the corresponding environment parameters.

The sound propagation calculated by the full-wave, pre-corrected fast Fourier transform accelerated ESM [6] and the proposed model is presented in Fig. 20 at a receiver depth of 20 m and shows conspicuous 3D effects including horizontal scattering, refraction, and diffraction, particularly in the vicinity of the sandbar region. Indeed, one can observe that the adiabatic approximation provided by the proposed model approaches the full-wave solution in most regions where horizontal refraction dominates the 3D effect. Overall, the proposed model predicts acceptable and promising results in terms of the energy distribution compared with the full-wave solution, with the overall errors plotted in the lower panel barely exceeding 5 dB over the range where horizontal refraction dominates. In the region where modal coupling is significant, it overlooks the oscillatory contour induced by the intricate mechanism of the modal energy transfer, thus showing larger errors up to 10 dB. However, this does not reflect any underlying issue associated with the proposed MOR technique for solving the HRE, and the differences from the full-wave solution are solely caused by the adiabatic approximation. Note that noticeable errors exceeding 20 dB appear over the range where troughs in the sound field occur, which cannot be attributed to the adiabatic approximation.

Table 3

CPU time and error analyses for the proposed MOR technique compared with the full-order model. The front annotated in red represents the time for mesh construction.

Test case	CPU time		Relative errors
	Full-order FEM	MOR model	
ASA wedge	8 min (6 min)	0.15 s	0.97%
Infinite cosine hill	8 h 9 min (3 h 1 min)	2.8 s	1.68%
Corrugated seabed	19 min 27 s (8 min 7 s)	3 min 20 s	2.58%
Realistic sandbar	17 min 53 s (7 min 23 s)	4 min	1.73%

3.4. Comparison with a full-order model for solving HREs

To assess the efficiency achieved by the proposed MOR technique, it is necessary to compare it with a full-order model. However, it is worth noting that, to the best of the author's knowledge, there is currently no full-order solver available for HREs. Historically, HREs have been tackled either through ray tracing or parabolic equation, neither of which constitutes a full-order model. Ray tracing provides a high-order asymptotic solution for Helmholtz-like HREs, while parabolic equation solves the paraxial form of HREs rather than the HREs themselves.

Here, we present a full-order model for solving HREs using the FEM. A detailed description of this model is provided in [Appendix A.2](#). The developed full-order FEM serves as a benchmark for comparing other methods used to solve HREs as well. For efficiency, only individual coefficient of the vertical mode is considered for each test case. [Table 3](#) presents the CPU time and error analyses compared with the full-order FEM for the coefficient of the first vertical mode. The results demonstrate that the proposed MOR technique is exceptionally efficient in the ASA wedge case and the infinite cosine hill case, particularly due to their longitudinal invariance, being over a thousand times faster than the full-order FEM. The significantly longer computation time required by the full-order FEM in the infinite cosine hill case is attributed to the mesh count exceeding 5×10^7 . Even in fully 3D cases, the proposed MOR technique remains 5–6 times faster than the full-order FEM. Overall, the errors relative to the full-order FEM are below 3%, indicating a significant speed-up achieved by the MOR technique without compromising accuracy.

4. Concluding remarks

This paper has presented an MOR technique designed to solve the HREs governing large-scale 3D underwater acoustic propagation. This technique projects the exact solution of the HRE onto a lower-dimensional space to reduce computational costs. Drawing inspiration from normal mode theory, we utilized the transverse eigenfunctions of the coefficients in the expansion over vertical modes to define this reduced space. Consequently, the original model, initially defined by discretization points along the transverse direction, is simplified into a lower-dimensional model based on transverse eigenfunctions. To address the corresponding eigenproblem, we incorporated two PMLs into the model to truncate the transverse directions of the horizontal domain. Subsequently, the transverse eigenfunctions were projected onto the space bounded by the outer PML boundaries. This projection yielded a closed generalized matrix eigenproblem, facilitating accurate determination of the corresponding eigenvalues and enabling wide-angle horizontal propagation angles covering $\pm 90^\circ$.

Longitudinally invariant environments exhibit a variably separative nature in which the transverse eigenfunctions of the coefficients of vertical modes remain uncoupled. This characteristic enables the simultaneous computation of modal coefficients across different x and y coordinates by solving the associated eigenproblem just once. Such efficiency renders the proposed MOR technique particularly effective in longitudinally invariant settings. Comparative analysis demonstrates that our MOR technique surpasses the state-of-the-art wide-angle mode parabolic equation, offering over 100 times faster computation and a broader angle solution. We validated the proposed MOR technique and investigated mode coupling effects in two longitudinally invariant scenarios: the ASA benchmark wedge and the infinite cosine hill.

We extended our MOR technique to fully 3D underwater scenarios by introducing an admittance matrix. This matrix was derived by formulating the HRE as a first-order evolution equation along the longitudinal range. Because horizontal wavenumbers depend on both the transverse and longitudinal ranges, the transverse eigenfunctions of modal coefficients become coupled. We addressed the coupled transverse eigenfunctions using an evolutionary Magnus scheme, a memory-saving strategy that prevents numerical overflow when the longitudinal range is large. Two fully 3D examples were used to validate the proposed MOR technique, including sound propagation over a corrugated seabed and realistic topography acquired from NOAA data. The proposed model enables efficient solutions on a coarse grid without compromising accuracy for fully 3D problems. While this article primarily focuses on solving HREs without modal interactions, it is worth noting that the proposed MOR technique could also serve as a MOR of the parabolic equation modal coupled system for 3D sound propagation [62], which will be the focus of our future work.

CRediT authorship contribution statement

Tengjiao He: Writing – original draft, Visualization, Validation, Software, Methodology, Investigation, Funding acquisition, Formal analysis, Conceptualization. **Juan Liu:** Writing – review & editing, Supervision, Investigation. **Shanjun Ye:** Visualization, Resources. **Xin Qing:** Writing – review & editing, Formal analysis. **Shiqi Mo:** Supervision, Funding acquisition.

Declaration of competing interest

The authors declare that they have no known competing financial interests or personal relationships that could have appeared to influence the work reported in this paper.

Data availability

Data will be made available on request.

Acknowledgments

This work was supported by the National Natural Science Foundation of China (Grant No. 12304499 and Grant No. 52271343) and the Stable Supporting Fund of the National Key Laboratory of Underwater Acoustic Technology (Grant No. JCKYS2023604 SSJS018). The authors would like to thank the two anonymous reviewers, whose helpful comments and suggestions have greatly improved the manuscript.

Appendix

A.1. Newton–Raphson iteration for determining eigenvalues of waterborne modes in a Pekeris waveguide

In a Pekeris waveguide, where a system of a two-layer fluid medium is considered, the dispersion equation to be solved is given by:

$$\tan \gamma_1 H = i \frac{\gamma_1}{b_{12} \gamma_2}, \quad (35)$$

where H is the water depth, b_{12} represents the density ratio of the water to the seabed, $\gamma_1 = \sqrt{k_1^2 - k_r^2}$, and $\gamma_2 = \sqrt{k_2^2 - k_r^2}$, where k_1 and k_2 are the wavenumber of the water and seabed, respectively. The dispersion equation can be expressed by:

$$\gamma_{1j} H = j\pi + \tan^{-1} \left[i \frac{\gamma_{1j}}{b_{12} \gamma_{2j}} \right]. \quad (36)$$

Writing γ_{2j} in terms of γ_{1j} gives:

$$\gamma_{2j} = -i \sqrt{k_1^2 - k_2^2 - \gamma_{1j}^2}. \quad (37)$$

Returning Eq. (36), one can rewrite the equation to be solved as:

$$F(X) = X - (j - 0.5)\pi - \tan^{-1}[g(X)], \quad (38)$$

where

$$\begin{aligned} X &= \gamma_{1j} H, \\ g(X) &= b_{12} \frac{\sqrt{\hat{a} - X^2}}{X}, \end{aligned} \quad (39)$$

and

$$\hat{a} = (k_1^2 - k_2^2)H^2. \quad (40)$$

The derivative of F can be given by:

$$\frac{dF}{dX} = 1 + \frac{1}{(1 + g^2)X} \left[g + \frac{b_{12}^2}{g} \right]. \quad (41)$$

Then, approximating the j th root as X_j yields:

$$X_{j+1} = X_j - \frac{F(X_j)}{F'(X_j)}. \quad (42)$$

Eq. (42) exhibits a rapid convergence just a few iterations to the solution, with an initial value of $X_0 = (j - 0.5)\pi$. The eigenvalues of waterborne modes then can be calculated quite straightforwardly once γ_{1j} are solved through the above iterative procedure, and that is:

$$k_{rj} = \sqrt{k_1^2 - \gamma_{1j}^2}. \quad (43)$$

After determining the eigenvalues, the mode shape function can be computed analytically using the complex depth approximation:

$$P_j(z) = L_j^{-1} \sin(\gamma_{1j} z). \quad (44)$$

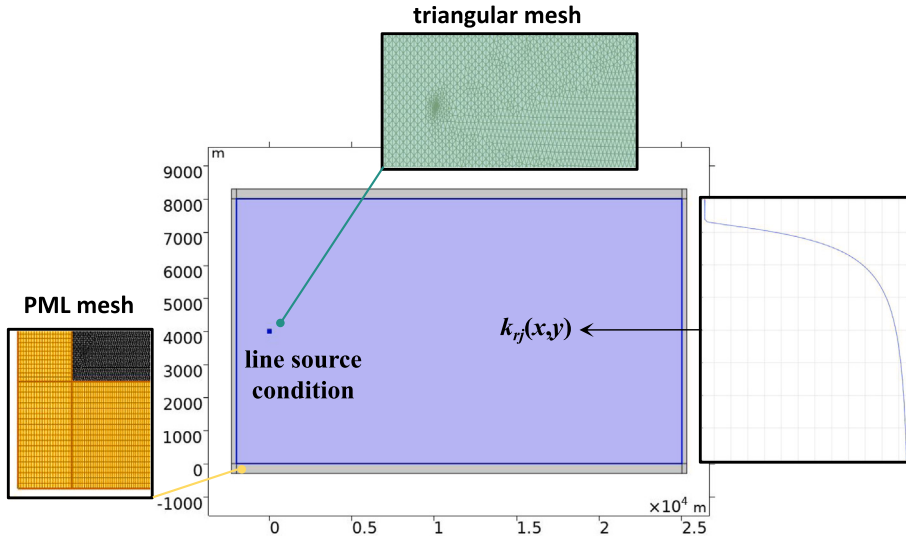


Fig. 21. The schematic of the full-order FEM implemented using the commercial software COMSOL.

where

$$L_j = \frac{H_e}{2} - \frac{\sin(2\gamma_{1j} H_e)}{4\gamma_{1j}} + b_{12} \frac{\sin(\gamma_{1j} H_e)^2}{2\gamma_{2j}}, \quad (45)$$

with $H_e = j\pi/\gamma_{1j}$.

A.2. Full-order finite element method for solving horizontal refraction equations

The fundamental approach involves discretizing the same computational domain treated in our MOR technique using free triangular meshes and solving the corresponding HREs using a 2D FEM scheme. The FEM solver was implemented using the commercial package COMSOL Multiphysics, employing a 2D frequency-domain solver for pressure acoustics. The modal horizontal wavenumbers k_{rj} are pre-computed and then utilized as input for the FEM-based HREs solver. The point-source excitation is imposed using the ‘line source’ condition in the 2D pressure acoustics module. The discretization scheme in the FEM ensures a minimal mesh size of $\lambda/5$, with a mesh density ten times higher at the source. Additionally, four PMLs are implemented to truncate both the x and y directions, each with a thickness of 5λ and discretized by 10 layers of mapping mesh, guaranteeing convergence of FEM results. Fig. 21 illustrates the schematic of the full-order FEM implemented using the commercial software COMSOL.

References

- [1] M.J. Isakson, B. Goldsberry, N.P. Chotiros, A three-dimensional, longitudinally-invariant finite element model for acoustic propagation in shallow water waveguides, *J. Acoust. Soc. Am.* 136 (2014) EL206–EL211, <http://dx.doi.org/10.1121/1.4890195>.
- [2] Z. Xie, R. Matzen, P. Cristini, D. Komatitsch, R. Martin, A perfectly matched layer for fluid-solid problems: Application to ocean-acoustics simulations with solid ocean bottoms, *J. Acoust. Soc. Am.* 140 (2016) 165–175, <http://dx.doi.org/10.1121/1.4954736>.
- [3] J. Lecoulant, T.C.A. Oliveira, Y.-T. Lin, Three-dimensional modeling of T-wave generation and propagation from a South Mid-Atlantic Ridge earthquake, *J. Acoust. Soc. Am.* 150 (2021) 3807–3824, <http://dx.doi.org/10.1121/10.0007072>.
- [4] W. Liu, L. Zhang, W. Wang, Y. Wang, S. Ma, X. Cheng, W. Xiao, A three-dimensional finite difference model for ocean acoustic propagation and benchmarking for topographic effects, *J. Acoust. Soc. Am.* 150 (2021) 1140–1156, <http://dx.doi.org/10.1121/10.0005853>.
- [5] C. Li, B.K. Campbell, Y. Liu, D.K. Yue, A fast multi-layer boundary element method for direct numerical simulation of sound propagation in shallow water environments, *J. Comput. Phys.* 392 (2019) 694–712, <http://dx.doi.org/10.1016/j.jcp.2019.04.068>.
- [6] T. He, S. Mo, E. Fang, M. Wang, R. Zhang, Modeling three-dimensional underwater acoustic propagation over multi-layered fluid seabeds using the equivalent source method, *J. Acoust. Soc. Am.* 150 (2021) 2854–2864, <http://dx.doi.org/10.1121/10.0006663>.
- [7] F.B. Jensen, W.A. Kuperman, M.B. Porter, H. Schmidt, A. Tolstoy, *Computational Ocean Acoustics*, Vol. 2011, Springer, 2011.
- [8] R.N. Baer, Propagation through a three-dimensional eddy including effects on an array, *J. Acoust. Soc. Am.* 69 (1981) 70–75, <http://dx.doi.org/10.1121/1.385253>.
- [9] Y.-T. Lin, T.F. Duda, A.E. Newhall, Three-dimensional sound propagation models using the parabolic-equation approximation and the split-step Fourier method, *J. Comput. Acoust.* 21 (2013) 1250018, <http://dx.doi.org/10.1142/S0218396X1250018X>.
- [10] F. Sturm, Leading-order cross term correction of three-dimensional parabolic equation models, *J. Acoust. Soc. Am.* 139 (2016) 263–270, <http://dx.doi.org/10.1121/1.4939735>.
- [11] K. Lee, W. Seong, Y. Na, Split-step Padé solver for three-dimensional cartesian acoustic parabolic equation in stair-step representation of ocean environment, *J. Acoust. Soc. Am.* 146 (2019) 2050–2057, <http://dx.doi.org/10.1121/1.5125592>.

- [12] K. Lee, W. Seong, Y. Na, Three-dimensional Cartesian parabolic equation model with higher-order cross-terms using operator splitting, rational filtering, and split-step Padé algorithm, *J. Acoust. Soc. Am.* 146 (2019) 2041–2049, <http://dx.doi.org/10.1121/1.5125428>.
- [13] Y.-T. Lin, Three-dimensional boundary fitted parabolic-equation model of underwater sound propagation, *J. Acoust. Soc. Am.* 146 (2019) 2058–2067, <http://dx.doi.org/10.1121/1.5126011>.
- [14] T.C.A. Oliveira, Y.-T. Lin, Three-dimensional global scale underwater sound modeling: The T-phase wave propagation of a Southern Mid-Atlantic Ridge earthquake, *J. Acoust. Soc. Am.* 146 (2019) 2124–2135, <http://dx.doi.org/10.1121/1.5126010>.
- [15] W. Liu, L. Zhang, W. Wang, Y. Wang, S. Ma, X. Cheng, W. Xiao, A three-dimensional finite difference model for ocean acoustic propagation and benchmarking for topographic effects, *J. Acoust. Soc. Am.* 150 (2021) 1140–1156, <http://dx.doi.org/10.1121/10.0005853>.
- [16] T.C.A. Oliveira, P. Nielsen, Y.-T. Lin, N. Kushida, S.M. Jesus, Megamer propagation and correlation of T-waves from Kermadec Trench and Islands, *Front. Mar. Sci.* 9 (2022) <http://dx.doi.org/10.3389/fmars.2022.1009013>.
- [17] Y.-T. Lin, Three-dimensional propagation of seismic airgun signals in the Mississippi Canyon area of the Gulf of Mexico, *JASA Express Lett.* 1 (2021) 026001, <http://dx.doi.org/10.1121/10.0003451>.
- [18] B.J. DeCourcey, Y.-T. Lin, Spatial and temporal variation of three-dimensional ship noise coherence in a submarine canyon, *J. Acoust. Soc. Am.* 153 (2023) 1042–1051, <http://dx.doi.org/10.1121/10.0017166>.
- [19] T.-T. Chen, Y.-T. Lin, L.Y.-S. Chiu, Impacts of seafloor characteristics on three-dimensional sound propagation in a submarine canyon, *JASA Express Lett.* 3 (2023) 016002, <http://dx.doi.org/10.1121/10.0016835>.
- [20] Y.-T. Lin, L.J. Van Uffelen, J.H. Miller, G.R. Potty, K.J. Vigness-Raposa, Horizontal refraction and diffraction of underwater sound around an island, *J. Acoust. Soc. Am.* 151 (2022) 1684–1694, <http://dx.doi.org/10.1121/10.0009672>.
- [21] M. Trofimov, A. Zakharenko, S. Kozitskiy, Mode Gaussian beam tracing, *Comput. Phys. Comm.* 207 (2016) 179–185, <http://dx.doi.org/10.1016/j.cpc.2016.06.002>.
- [22] P.S. Petrov, M. Ehrhardt, A.G. Tyshchenko, P.N. Petrov, Wide-angle mode parabolic equations for the modelling of horizontal refraction in underwater acoustics and their numerical solution on unbounded domains, *J. Sound. Vib.* 484 (2020) 115526, <http://dx.doi.org/10.1016/j.jsv.2020.115526>.
- [23] M.D. Collins, The adiabatic mode parabolic equation, *J. Acoust. Soc. Am.* 94 (1993) 2269–2278, <http://dx.doi.org/10.1121/1.407498>.
- [24] P.S. Petrov, F. Sturm, An explicit analytical solution for sound propagation in a three-dimensional penetrable wedge with small apex anglea, *J. Acoust. Soc. Am.* 139 (2016) 1343–1352, <http://dx.doi.org/10.1121/1.4944692>.
- [25] P. Petrov, S. Prants, T. Petrova, Analytical Lie-algebraic solution of a 3D sound propagation problem in the ocean, *Phys. Lett. A* 381 (2017) 1921–1925, <http://dx.doi.org/10.1016/j.physleta.2017.04.011>.
- [26] P.N. Petrov, P.S. Petrov, Asymptotic solution for the problem of sound propagation in a shallow sea with the bathymetry described by a parametric quadratic function, *J. Acoust. Soc. Am.* 146 (2019) 1946–1955, <http://dx.doi.org/10.1121/1.5125593>.
- [27] A.C. Antoulas, *Approximation of Large-Scale Dynamical Systems*, SIAM, 2005.
- [28] P. Benner, M. Ohlberger, A. Cohen, K. Willcox, *Model Reduction and Approximation: Theory and Algorithms*, SIAM, 2017.
- [29] P. Benner, W. Schilders, S. Grivet-Talocia, A. Quarteroni, G. Rozza, L. Miguel Silveira, *Model Order Reduction: Volume 3: Applications*, De Gruyter, 2020.
- [30] P. Benner, W. Schilders, S. Grivet-Talocia, A. Quarteroni, G. Rozza, L. Miguel Silveira, *Model Order Reduction: Volume 2: Snapshot-Based Methods and Algorithms*, De Gruyter, 2020.
- [31] A.T.P. Silke Glas, K. Urban, A reduced basis method for the wave equation, *Int. J. Comput. Fluid. D* 34 (2020) 139–146, <http://dx.doi.org/10.1080/10618562.2019.1686486>.
- [32] C. Bigoni, J.S. Hesthaven, Simulation-based anomaly detection and damage localization: An application to structural health monitoring, *Comput. Methods Appl. Mech. Eng.* 363 (2020) 112896, <http://dx.doi.org/10.1016/j.cma.2020.112896>.
- [33] J. Henning, D. Palitta, V. Simoncini, K. Urban, An ultraweak space-time variational formulation for the wave equation: Analysis and efficient numerical solution, *ESAIM Math. Model. Numer. Anal.* 56 (2022) 1173–1198.
- [34] X. Xie, Y. Liu, Efficient multi-frequency solutions of FE-BE coupled structural-acoustic problems using Arnoldi-based dimension reduction approach, *Comput. Methods Appl. Mech. Eng.* 386 (2021) 114126, <http://dx.doi.org/10.1016/j.cma.2021.114126>.
- [35] D. Panagiotopoulos, E. Deckers, W. Desmet, Krylov subspaces recycling based model order reduction for acoustic BEM systems and an error estimator, *Comput. Methods Appl. Mech. Eng.* 359 (2020) 112755, <http://dx.doi.org/10.1016/j.cma.2019.112755>.
- [36] X. Xie, W. Wang, K. He, G. Li, Fast model order reduction boundary element method for large-scale acoustic systems involving surface impedance, *Comput. Methods Appl. Mech. Eng.* 400 (2022) 115618, <http://dx.doi.org/10.1016/j.cma.2022.115618>.
- [37] X. Xie, Q. Zuo, H. Chen, Y. Xu, Z. Yi, K. He, A non-intrusive model order reduction boundary element method for frequency sweeps of 2D acoustics, *J. Sound. Vib.* 544 (2023) 117396, <http://dx.doi.org/10.1016/j.jsv.2022.117396>.
- [38] R. Hawkins, M.H. Khalid, K. Smetana, J. Trampert, Model order reduction for seismic waveform modelling: inspiration from normal modes, *Geophys. J. Int.* 234 (2023) 2255–2283, <http://dx.doi.org/10.1093/gji/ggad195>.
- [39] J.-P. Berenger, A perfectly matched layer for the absorption of electromagnetic waves, *J. Comput. Phys.* 114 (1994) 185–200, <http://dx.doi.org/10.1006/jcph.1994.1159>.
- [40] T. He, S. Mo, W. Guo, E. Fang, Modeling propagation in shallow water with the range-dependent sea surfaces and fluid seabeds using the equivalent source method, *J. Acoust. Soc. Am.* 149 (2021) 997–1011, <http://dx.doi.org/10.1121/10.0003385>.
- [41] T. He, X. Liu, R. Nie, W. Guo, S. Mo, B. Wang, Semi-analytical solution for sound propagation from a moving directional source in a shallow-water waveguide, *J. Sound. Vib.* 576 (2024) 118259, <http://dx.doi.org/10.1016/j.jsv.2024.118259>.
- [42] V. Pagneux, Multimodal admittance method in waveguides and singularity behavior at high frequencies, *J. Comput. Appl. Math.* 234 (2010) 1834–1841, <http://dx.doi.org/10.1016/j.cam.2009.08.034>.
- [43] Q. Li, J. Liu, W. Guo, Sound propagation in inhomogeneous waveguides with sound-speed profiles using the multimodal admittance method, *Chin. Phys. B* 29 (2020) 014303, <http://dx.doi.org/10.1088/1674-1056/ab5940>.
- [44] J. Liu, Q. Li, Coupled mode sound propagation in inhomogeneous stratified waveguides, *Appl. Sci.-Basel* 11 (2021) <http://dx.doi.org/10.3390/app11093957>.
- [45] J. Schiff, S. Shnider, A natural approach to the numerical integration of riccati differential equations, *SIAM J. Numer. Anal.* 36 (1999) 1392–1413, <http://dx.doi.org/10.1137/S0036142996307946>.
- [46] C. Budd, A. Iserles, A. Iserles, S. Nørsett, On the solution of linear differential equations in lie groups, *Phil. Trans. R. Soc. A* 357 (1999) 983–1019, <http://dx.doi.org/10.1098/rsta.1999.0362>.
- [47] B.J. DeCourcey, T.F. Duda, A coupled mode model for omnidirectional three-dimensional underwater sound propagation, *J. Acoust. Soc. Am.* 148 (2020) 51–62, <http://dx.doi.org/10.1121/10.0001517>.
- [48] I. Singer, E. Turkel, A perfectly matched layer for the Helmholtz equation in a semi-infinite strip, *J. Comput. Phys.* 201 (2004) 439–465, <http://dx.doi.org/10.1016/j.jcp.2004.06.010>.
- [49] D. Rabinovich, D. Givoli, E. Bécache, Comparison of high-order absorbing boundary conditions and perfectly matched layers in the frequency domain, *Int. J. Numer. Methods Biomed. Eng.* 26 (2010) 1351–1369, <http://dx.doi.org/10.1002/cnm.1394>.
- [50] J. Waldvogel, *Fast construction of the Fejér and Clenshaw-Curtis quadrature rules*, *BIT* 46 (2006) 195–202.
- [51] T. He, V.F. Humphrey, S. Mo, E. Fang, Three-dimensional sound scattering from transversely symmetric surface waves in deep and shallow water using the equivalent source method, *J. Acoust. Soc. Am.* 148 (2020) 73–84, <http://dx.doi.org/10.1121/10.0001522>.

- [52] G. Babkin, V. Klyatskin, Invariant imbedding method for wave problems, *Wave Motion* 4 (1982) 195–207, [http://dx.doi.org/10.1016/0165-2125\(82\)90019-1](http://dx.doi.org/10.1016/0165-2125(82)90019-1).
- [53] O. Gulin, Calculation of low-frequency sound fields in irregular waveguides with strong backscattering, *Acoust. Phys.* 54 (2008) 495–505.
- [54] M. Kazak, K. Koshel, P. Petrov, Generalized form of the invariant imbedding method and its application to the study of back-scattering in shallow-water acoustics, *J. Mar. Sci. Eng.* 9 (2021) <http://dx.doi.org/10.3390/jmse9091033>.
- [55] A. Iserles, A. Marthinsen, S. Nørsett, On the implementation of the method of Magnus series for linear differential equations, *BIT* 39 (1999) 281–304.
- [56] J.-B. Doc, S. Félix, B. Lihoreau, Coarse-grid computation of the one-way propagation of coupled modes in a varying cross-section waveguide, *J. Acoust. Soc. Am.* 133 (2013) 2528–2532, <http://dx.doi.org/10.1121/1.4799021>.
- [57] M.J. Buckingham, E.M. Giddens, Theory of sound propagation from a moving source in a three-layer Pekeris waveguide, *J. Acoust. Soc. Am.* 120 (2006) 1825–1841, <http://dx.doi.org/10.1121/1.2258095>.
- [58] M.B. Porter, The KRAKEN Normal Mode Program (Draft), Naval Research Laboratory, Washington DC, 1992.
- [59] E.K. Westwood, C.T. Tindle, N.R. Chapman, A normal mode model for acousto-elastic ocean environments, *J. Acoust. Soc. Am.* 100 (1996) 3631–3645, <http://dx.doi.org/10.1121/1.417226>.
- [60] T.C.A. Oliveira, Y.-T. Lin, M.B. Porter, Underwater sound propagation modeling in a complex shallow water environment, *Front. Mar. Sci.* 8 (2021) <http://dx.doi.org/10.3389/fmars.2021.751327>.
- [61] B.W. Eakins, Digital elevation model of Montauk, New York procedures, data sources and analysis, 2009.
- [62] P.S. Petrov, M. Ehrhardt, S.B. Kozitskiy, A generalization of the split-step Padé method to the case of coupled acoustic modes equation in a 3D waveguide, *J. Sound. Vib.* 577 (2024) 118304, <http://dx.doi.org/10.1016/j.jsv.2024.118304>.